Autogenic vs Subsidence Controls on Grain Size Fining through Multi-Channel Landscape Evolution Modelling

Amanda Lily Wild[1,2], Jean Braun[1,2], Alexander C Whittaker[3], and Sebastien Castelltort[4]

[1] Helmholtz Center Potsdam, GFZ German Center for Geoscience, Potsdam, Germany
[2]Universität Potsdam, Potsdam, Germany
[3]Royal School of Mines, Imperial College London, London, United Kingdom
[4]Department of Earth Sciences, University of Geneva, Rue des Maraîchers 13, 1205 Genève, Switzerland

Correspondence: Amanda Lily Wild (awild@gfz-potsdam.de)

Abstract. Within the stratigraphic record, changes in grain size are often interpreted as a signature of external forcing events. However, it is not yet well constrained how autogenic processes (such as channel mobility) influence grain size signatures within the fluvial system. Here, we combine a landscape evolution model based on the Stream Power Law but modified for sedimentation (Yuan et al., 2019) with an extension of the self-similar grain size model Fedele and Paola (2007) to multiple

5 dimensions (i.e., along dynamically evolving river channels) to study the relative importance of autogenic processes in controlling grain size fining. We first show how our new model can reproduce the results obtained by classical analytical solutions assuming that fining is controlled by subsidence only, in a single or amalgamated channel. We then show that deviations from past (subsidence and single channel only) predictions arise when varying two main parameters: first the ratio between the incoming sediment flux and integrated subsidence rate (F), which increases with the degree of bypass of the system; and second,

10 the ratio of the discharge leaving the mountain to the discharge generated within the subsiding basin (β), which controls the shape of the topography of the basin. We demonstrate that there exists two regimes, one corresponding to low values of F or high values of β, where the grain size fining is controlled by subsidence, and one corresponding to high F and low β values, where grain size fining is controlled by autogenic processes under steep topographic slopes that propagate sedimentary waves through the basin. Coupling the LEM to a flexural model predicts that grain size fining evolves from subsidence to autogenic-

15 control in basins characterized by a progressive increase of F (under-filled to over-filled foreland), as seen in the case example of the Alberta Foreland Basin. Our results indicate that grain size fining during low filling conditions (e.g. early stage as the basin is forming) can indicate the dominantly tectonic controlled parameter of the flux relative to underlying subsidence ratio (F); whereas, any fining under high bypass conditions (e.g. late stage once the basin is overfilled) can indicate the climate controlled upstream vs downstream ratio (β).

20 **Plain Language Summary:** Grain size deposited within fluvial channels forms the stratigraphic record, which has been used to interpret tectonic events, basin subsidence, and even changes in precipitation long after ancient mountain chains have eroded away. For the first time, our work combines past equations for modelling fluvial grain size fining based on deposition rates and sediment flux with a landscape evolution model allowing for sediment interactions. Such a landscape evolution model can depict the change in topography (through erosion and deposition) within the orogen and

25   basin over long (kyr-Myr) time scales. Past applications for stratigraphic grain size did not consider the topography or multi-channel dynamics that a landscape evolution model can predict. Our work identifies under what basin geometries, precipitation gradients, basin filling and other multi-channel and topographic dynamics most impact the stratigraphic grain size record and cause deviations from past applications of grain size fining. This has implications for the application and interpretation of climatic and tectonic signals within the stratigraphic record. We also provide real world examples

30   (such as in the Alberta Basin) to compare with our model.

1 Introduction

The grain size (GS) preserved within the stratigraphic record over thousands to millions of years has applications for the generation of reservoirs for industrial applications or in recording significant geological climatic, eustatic, and tectonic events.

35   When used within their geologic context, variations in grain sizes can be used to identify changes in past environmental conditions that have been recorded in the stratigraphic record (Armitage et al., 2011; Rice, 1999). As described by Allen et al. (2013) and Duller et al. (2010), the ratio of sediment flux (driven by tectonics and climate) to accommodation controls basin filling, deposition, subsequent fan development, and downstream fining for gravel and sand coarse fractions. However, there are a number of internal dynamical processes [1] and emergent drainage and topographic properties that impact the coarse

40   grain size record depending on the proportional relationships of flux, discharge, accommodation space, and basin geometries triggered by external forcing (Sømme et al., 2009; Scheingross et al., 2020; Romans et al., 2016; Hajek and Straub, 2017). For example, increasing precipitation duration and magnitude within the source catchment results in a lateral shift in where coarser grains are deposited in the system and a lengthening of the fan area in response to the accompanying increase in sediment flux (Armitage et al., 2011). In terms of a tectonic control, Hooke (1968) suggests that higher tectonic uplift and tilting within

45   the Panamint Range produce higher flux in the western part of Death Valley leading to more extensive coarse grained alluvial fans relative to the eastern Black Mountains area. Within a basin, grain size fining rate is more rapid in high amplitude and short wavelength subsidence regimes (Duller et al., 2010) as observed by Dingle et al. (2016) within the Ganga Plain. The examples above highlight how a thorough understanding of grain size fining in response to external forcing with consideration of autogenic dynamics over long timescales (Myr) has broad implications for interpreting the sedimentary record to unravel

50   tectonic conditions and climates of the geological past.

    It is only over the past few decades that efforts have emerged to disentangle the impact of autogenic dynamics (interchangeably referred to as internal dynamics) on the sediment record despite centuries of research on the impact of external forcing. In general, sediment recycling and autogenic dynamics are associated with short to intermediate time scales, transfer zones,

---

[1]Internal or Autogenic dynamics are feedbacks between topography, erosion, and sediment transport that occur independent of external perturbations such as basin reorganization, sediment waves, channel avulsions, knickpoint generation, and more (Scheingross et al., 2020).

and with response times smaller than those associated with external perturbations (Scheingross et al., 2020). However, due to
55 its impact on erosion and deposition rates, autogenic dynamics (for example, channel mobility) can end up impacting the Myr
timescales and potentially interact with external forcing signals (Scheingross et al., 2020). The impact of autogenic dynamics
on preservation can be important and counter-intuitive: (Hill et al., 2012) has shown, for example, that, in certain scenarios,
external signals may be better recorded when only 40 percent of the sediment is preserved compared to systems characterized
by 90 percent preservation due to less complex drainage reorganization and internal dynamics. Similarly, Straub and Esposito
60 (2013) introduce a ratio of vertical aggregation relative to lateral mobility/variation that they say controls stratigraphic com-
pleteness, whereby higher discharge and higher sedimentation rate leads to lower reworking and enhanced preservation. This
behaviour results from the fact that autogenic processes react to external forcing. These processes (such as channel avulsion or
depositional pulses) alter and redistribute the energy of an external event, at times shredding it, within the stratigraphic record,
but these responses are often not considered when interpreting climatic or tectonic signals.

65   Alluvial fans and adjacent plains are quintessential landscape features where selective deposition of coarse grains (gravel
and sand) from a source catchment can be readily observed and, due to abundant sediment and dynamic reorganization, both
locations can be highly influenced by internal dynamics. As depositional features, alluvial fans are impacted by variations in
accommodation and sediment flux that influence grain size fining (Duller et al., 2010; Whittaker et al., 2011) and thus, at the
landscape scale, fan and coarse grain size propagation extents tend to mirror one another (Bull, 1977; Hooke, 1968; Price,
70 1974; Parker et al., 1998; Drew, 1873; Blair and McPherson, 1994). The topographic slope and extent of the fans can have an
influence on drainage dynamics (such as transitioning from sheet to channelized rill flow leaving the fan) and the subsequent
propagation of coarse grains evenly or dispersed into the basin (Bull, 1977). Precipitation and its contribution to active channel
discharge also play an important role in controlling transport capacity, and variations in precipitation both temporally and
spatially (in particular between the upstream catchment and the basin area hosting the fan) are likely to impact grain size
75 fining and fan size. There has long been observations of a strong correlation between fan area or gradients and catchment area
(Bull, 1977; Hooke, 1968; Blair and McPherson, 1994). Recently, Braun et al. (2023) have shown, using modeling and remote
sensing examples, that the established (e.g., Bull, 1977) correlation between fan and catchment area can be improved when the
gradient of precipitation between the catchment and the basin is considered.

    Foreland basins are larger-scale geological features that combine many of the depositional environments (fans, channels,
80 and flood plain) and processes (accommodation, bypass, and subsidence) mentioned above. Their subsidence is controlled by
flexure of the lithosphere under the weight of an adjacent mountain belt, and they are filled by the product of the erosion
of that mountain. As collision proceeds and the mountain grows, the incoming flux and subsidence within the basin evolve
with time (Covey, 1986; DeCelles and Giles, 1996; Catuneanu, 2004; Beaumont, 1981), which strongly influences coarse
grain size fining and stratigraphic preservation. For example, Cant and Stockmal (1989); Mossop and Shetsen (1994); Poulton
85 et al. (1990) described in these terms the stratigraphic evolution of the Western Canada foreland basin as it transitions from
flysch to molasse and the main depositional depocentre migrates back and forth to the northwest and southeast as the basin
progressively fills and progresses into bypass. In a more theoretical study, Duller et al. (2010) showed how grain size fining
decreases and coarse grains propagate further into the basin as the system transitions into higher bypass. Not all systems

reach bypass depending on the accommodation space, but under the right conditions, basins will fill over time. In addition to
evolving flexural response within a basin, catchments can also experience drainage divide capture/loss (Bernard et al., 2021),
regional/local climatic responses (e.g., glacial accretion or loss depending on aspect and sun exposure) (Lai and Huppert,
2023) or develop precipitation gradients (e.g., orographic lift developing as the mountain height increases with time to a
steady-state) (Leonard and Whipple, 2021) as the orogen evolves; these phenomena would influence the transient sediment
flux and discharge to the basin, which could subsequently influence drainage dynamics and coarse grain propagation signals
into the basin (Leeder et al., 1998).

Geomorphologists and modellers tend to separate river systems into detachment[2] and transport[3] limited systems (Whipple and Tucker, 2002). Fans and fluvial dominated depositional basins have largely been considered purely transport-limited
(Henderson, 1966; Flemings and Jordan, 1989; Armitage et al., 2011; Paola et al., 1992) or some combination of detachment
and transport limited (Davy and Lague, 2009; Braun, 2022; Simpson and Castelltort, 2006) whereas research has suggested
transport limited conditions are more dominant within the basin in most natural systems (Guerit et al., 2019). The impact
of autogenic dynamics on residence times or stratigraphic shredding are a phenomenon more commonly discussed within
transport-limited, sedimentary basins (Romans et al., 2016; Sømme et al., 2009; Tofelde et al., 2021). Channel and sedimentary dynamics, such as avulsions, are one type of phenomena common to a transport-limited basin that can impact the entire
system and control where coarse grains are deposited. Stouthamer and Berendsen (2007) have shown that changes in avulsion
frequency and associated sediment dispersion on the Rhine-Meuse delta can be related to changes in sea-level, human influence, climate, and tectonics. The same authors showed that avulsions on the Rhine-Meuse delta, lead to other internal dynamic
cycles where infilling initiates at the delta toe and progressively migrate upstream in a sediment wave within the system until
they reach the delta apex which triggers another avulsion to initiate (Stouthamer and Berendsen, 2007).

Modeling is one way to untangling the impact of internal and external forcing feedback on the grain size of the stratigraphic
record, but requires a reduced complexity framework as certain hydraulic details of the modern system are too complex to
model over millions of years and, for most, are not preserved within the geologic record. Sedimentologists have used reduced
complexity models of long-term grain size fining in so-called source to sink approaches to reproduce and thus interpret the
sedimentological record (Veldkamp et al., 2017; Carretier et al., 2016; Armitage et al., 2011; Davy and Lague, 2009; Paola and
Voller, 2005). Fedele and Paola (2007), for example, have developed a reduced complexity model of depositional controlled
grain size fining using concepts suggested by and derived from the stratigraphic record such as time-integrated grain size self-similarity, avoiding the need for local fine-scale hydrology details (not preserved over long-timescales). The self-similarity
based grain size fining model assumes that downstream deposition is the main control on the fining rate (Fedele and Paola,
2007) and, thus, does not consider feedbacks between grain size and topography or the influence of abrasion. [4]

Applications of Fedele and Paola (2007) grain size fining approach by Duller et al. (2010), Whittaker et al. (2011), and
others have assumed that deposition is equal to subsidence and that fining is limited to the active channel. Although some

---

[2]sediment supply or ability to incise/weather as the major limiting factor

[3]ability to transport away abundant sediment as the major limited factor

[4]See (Fedele and Paola, 2007) for a full description of model assumptions, limitations, and mechanics.

approaches include fan width (D'Arcy et al., 2017), these applications do not include autogenic dynamics and multi-channel interactions. Consequently, in these approaches, the grain size fining rate can be used to estimate the subsidence distribution of sedimentary basins, assuming the volumetric distribution of sedimentation can be reconstructed. However, in addition to external forcing (i.e., climate and tectonics), grain size trends are influenced by autogenic dynamics (such as avulsions or

125 drainage re-organization) that will alter erosion and depositional patterns Hajek and Straub (2017). Channel mobility in particular is not captured in past applications of Fedele and Paola (2007)'s grain size self-similar model and would break Duller et al. (2010)'s assumption of uniform deposition rate across the basin. However, applying Fedele and Paola (2007)'s equations within an evolving foreland basin including multiple channel dynamics would allow for the analysis of autogenic processes on stratigraphic grain size preservation in a way previously disregarded.

130 This work presents a new method (that we shall call GravelScape) that generalizes Fedele and Paola (2007)'s self-similar gravel grain size model into multiple dimensions (downstream, across the basin, and overtime/depth) using Braun and Willett (2013) landscape evolution model (FastScape) with a depositional term from Yuan et al. (2019). Since the deposition rate is calculated directly within FastScape (deposition is critical to Fedele and Paola (2007)'s grain size approach), the assumption of Duller et al. (2010) and Whittaker et al. (2011) that the sedimentation rate is equal to subsidence rate is no longer required. The

135 GravelScape approach also moves away from any length scaling allowing for ease of application across multiple dimensions and methods. Using GravelScape we demonstrate the role of across basin dynamics on grain size fining through a sensitivity analysis and comparison with Duller et al. (2010). For this, we performed a series of simple numerical experiments to predict grain size fining rate in sedimentary systems of varying fluxes and geometries that are fed by an orogenic source area and undergoing subsidence at a prescribed rate. In this way, GravelScape is able to quantify the impact of external and autogenic

140 (multi-channels) dynamics on grain size fining in a way that was previously not possible along a single river long profile.

Another advantage of the GravelScape method is the incorporation of flexure. After validating the approach under a single channel or sheet flow hypothesis (1D profile) and with multiple channels (2D) using a prescribed subsidence curve, we apply the grain size model to a sample basin where subsidence is the result of isostatic flexure under the load of the growing mountain source area. We show that the resulting patterns of grain size fining through flexural control on the deposition of sediments

145 within the basin are not dissimilar to the stratigraphic record observed in the western Canada foreland basin (Catuneanu, 2004; Cant and Stockmal, 1989; Mossop and Shetsen, 1994). Finally, we demonstrate, using GravelScape, how we can better predict under which conditions autogenic (across basin) channel dynamics are the most efficient in altering the grain size record.

2 Model Descriptions

2.1 The Landscape Evolution Model (LEM)

150 We use FastScape (Bovy, 2021) as a basic Landscape Evolution Model (LEM) that solves the Stream Power Law (SPL) in two dimensions following the efficient algorithm described in Braun and Willett (2013). The SPL states that the rate of bedrock elevation change is the sum of uplift rate U and erosion rate assumed proportional to upstream drainage area, A, used as a

proxy for discharge, and local slope S (Whi) :

$$\frac{dh}{dt} = U - KA^m S^n \tag{1}$$

155   K is a rate coefficient or erosivity that depends mostly upon basin lithology and precipitation rate. m and n are SPL exponents that generally maintain a ratio of $m/n = 0.5$. Sediment transport and deposition are incorporated into FastScape by using Yuan, Braun, Guerit, Rouby, and Cordonnier (2019)'s implementation of Davy and Lague (2009)'s $\xi - q$'s algorithm which states that the rate of sediment deposition is proportional to sediment flux and inversely proportional to upstream drainage area. This leads to the following evolution equation that integrates the processes of erosion, transport, and deposition into a simple

160   framework:

$$\frac{dh}{dt} = -K\tilde{p}^m A^m \left(\frac{dh}{ds}\right)^n + \frac{G}{\tilde{p}A} \int_A \left(U - \frac{dh}{dt}\right)dA \tag{2}$$

In this formulation, G is a dimensionless deposition coefficient and $\tilde{p}$ represents spatial or temporal variations in precipitation rate with respect to a mean value that is contained in both K and G. We will vary G and discuss its impact on model results. G controls the transport (G over 0.4) or detachment (G under 0.4) limited nature of the depositional system (Yuan et al., 2019).

165   Guerit et al. (2019) has demonstrated that many natural river systems tend to be on the transport limited side (G = 0.7). More detachment limited systems tend to represent more fine-grained rivers or coarse systems that are supply limited (e.g., flushed of their sediment supply faster than it can be generated). Transport limited systems tend to represent more coarse-grained rivers and systems with abundant available sediment. Note that, for numerical reasons, G=1 is the maximum transported-limited value computed efficiently and reliably by FastScape (Yuan et al., 2019).

170   In FastScape, in order to compute transport of water and sediment, nodes are ordered along flow paths through the landscape. This is performed by creating a stack order using single or multi-flow algorithms (See the supplementary materials for a comparison of single and multiple flow routing within FastScape). Note that single flow routing is an algorithm within FastScape that still has multiple channels, but with less or more simplified convergences and this is not the same as the single channel (eg: limits the across basin cells of the model to physically only produce one channel as shown in Fig. A2E) set-up that we will

175   describe later. In the single flow routing approach, each node has a single downhill receiver and channels can only converge (Braun and Willett, 2013). Alternatively, in the multi-flow approach (used in this work), each node may have multiple receivers such that the dynamics of a river diverging into multiple channels and converging downstream can be captured. As shown later in this work, subsidence rate can be imposed (see validation) or calculated in real time based on the flexural properties (see results) of the assumed underlying elastic plate. In the multi-flow case used throughout this work, the relative proportion of

180   water and sediment flux to each potential receiver is assumed proportional to slope.

2.1.1   Fedele and Paola (2007)'s Self-similarity based Grain Size Model

The underlying approach for our integration of grain size into a landscape evolution model is based on Fedele and Paola (2007)'s grain size (D) solution as a function of dimensionless distance downstream (x^*) within a depositional area for gravel:

185 $$D(x^*) = \overline{D_0} + \phi_0 \frac{C_2}{C_1} e^{-C_1 y^*} - 1 \tag{3}$$

and sand:

$$D(x^*) = \overline{D_0} e^{-C_3 y^*}. \tag{4}$$

where x^* is the distance along the river profile, x, scaled by its total length ($x^* = x/L$). $\overline{D_0}$ and ϕ_0 are the initial mean grain size and standard deviation at the source, respectively. $C_1, C_2,$ and C_3 are constants that represent the change in mean grain size
190 and standard deviation downstream, and often fall between 0.5-0.9 for C_1 and 0.1-0.45 for C_3. C_v is defined as the ratio of the downstream change in the standard deviation relative to mean grain size, i.e., $C_v = C_1/C_2$, and referred to as the coefficient of variation. C_v ranges, typically, between 0.7 and 0.9 (Fedele and Paola, 2007). Whittaker et al. (2011) note that a C_v value of 0.8 is common. Described further in Fedele and Paola (2007), y^* is the dimensionless distance transformation defined as:

$$y^*(x^*) = \int\limits_0^{x^*} R^*(x^*) \, dx^* \tag{5}$$

195 where R^* is the dimensionless downstream distribution of deposition defined as:

$$R^* = (1 - \gamma_p) RL. \tag{6}$$

where γ_p is the porosity of the sediment deposit, and R is the ratio of deposition rate, r, to sediment flux, q_s, i.e., $R = r/q_s$. At each x^* point along the river profile, R^* relates the sediment deposition into the substrate to the sediment flux in the river, taking into account a given length and porosity. Finally, deposition rate, r, is the sum of the rate of change of elevation of the
200 landscape and the subsidence rate, σ, i.e., $r = dh/dt + \sigma$.

To avoid repetition, this work will focus on the application of the gravel equation (3), but all methods described further below could be modified and applied to solving the sand equation (4). Put into words, grain size fining over long time spans using Fedele and Paola (2007)'s approach is said to be controlled by 1) the source sediment supply and grain size distribution, 2) the deposition throughout the system length, and 3) the hydraulic mobility of different grain size types (gravel vs. sand) with
205 an assumption of a constant shield stress at the bed, 4) self-similarity between the subsurface and surface of the distribution of gravel grain size clasts, and 5) a mass balance of the transport, substrate, and active layer (Fedele and Paola, 2007).

2.1.2 GravelScape: Incorporating the Self-Similar Grain Size Model into FastScape

Here, we propose a generalization of Fedele and Paola (2007)'s self-similar approach to two dimensions, i.e., following flow path or the stack node ordering computed in FastScape. We call our algorithm GravelScape. For this, we replace any spatial
210 integration or differentiation along the normalized river distance by its equivalent along the normalized steepest descent flow path, $s^* = L_s$, where L_s is the total length of the flow path. For example, the deposition rate is the spatial derivative of the flux along that flow path:

$$\frac{\partial q_s}{\partial s} = \frac{1}{L} \frac{\partial q_s}{\partial s^*} \tag{7}$$

In practice, we first compute the flow path and erosion/deposition rate along the flow path using the multi-flow routing in
215 FastScape. Next, sediment flux is computed by summing the erosion/deposition rate, r, down the flow path. Note that r is
negative where deposition takes place and will decrease the sediment flux q_s in the subsequent summation along the flow path
to the limit of $q_s = 0$. Once q_s is computed, the downstream distribution of deposition R can be calculated according to:

$$R = \begin{cases} (1 - \gamma_p)\frac{r}{q_s} & \text{if } r, q_s > 0 \\ 0 & \text{otherwise} \end{cases} \tag{8}$$

Next, the dimensionless distance transformation y^* is computed from a weighted summation of R through the drainage stack.
220 Where flow convergences (within multi-flow routing in FastScape), a weighted mean is used to compute the receiver y^*-values
where the weights are proportional to the upstream drainage area size of the donor nodes. In this way, when multiple flow paths
converge, the largest drainage area flow path will dominate the downstream grain size distribution. Such an approach matches
observations that grain size distributions of larger catchment rivers tend to dominate downstream grain size distributions (Har-
ries et al., 2019).

225 Finally, from y^* we compute the mean grain size using equation 3 or 4. In these equations, the value for D_0 is needed at
every grid point within the model. For this we compute a field D_0 that is obtained by propagating down the flow path of a
given time step, the value of the grain size last deposited on the bed (i.e., the initial value associated to the bedrock in the first
step or whatever was deposited last (D_t also referred to as DTime) in subsequent steps) where the channel originates. Using
D_0 defined in this way at each grid point, we use equations 3 or 4 to calculate a grain size value, D_x, at all points of the grid,
230 which we also use to update D_t for the following time step. At the start of the simulation, D_0 and D_t are set equal to the mean
grain size as produced by bedrock erosion in the mountain catchment. Note that deposition does not take place at every grid
point at every time step. So D_t is only updated to the newly computed grain size D_x where net deposition takes place. We carry
three grain size values at every grid point: (1) the grain size of material deposited at the current time step (D_x), (2) the grain
size at the surface of the model, i.e., of the material last deposited at that point (D_t) and (3) the grain size in the 'source' area,
235 i.e., where the flow path traversing the grid point originated (D_0). See supplementary materials for a comparison of single and
multi-flow routing D_0, D_t, and D_x for a given time step, as the results will only display the multi-flow GravelScape D_t and
D_x.

3   Modelling Approach: Past GS Applications, New LEM Additions, and Setup

3.1   Past Applications of Self-Similar Grain Size: Informing Validation

240 Past applications of (Fedele and Paola, 2007)'s self-similar grain size (eg: Duller et al. (2010) and Whittaker et al. (2011)) will
be used to validate the initial results using FastScape. Since, according to the self-similar model, grain size fining occurs where
deposition takes place, accommodation space needs to be generated within the model to produce fining. Duller et al. (2010)
and Whittaker et al. (2011) applied the Fedele and Paola (2007)'s self-similar model in a single downstream long profile to
derive the subsidence patterns of the basin at the time of the deposition (Eocene) of the Montsor fan deposits of the southern

245   Spanish Pyrenees. They conducted a robust sensitivity analysis on the impact of different subsidence characteristics on Fedele
and Paola (2007) grain size solutions. Through their approaches, Duller et al. (2010) and Whittaker et al. (2011) state that grain
size fining can be used to infer deposition rate and, thus, subsidence rate.

Already the Duller et al. (2010) and Whittaker et al. (2011) approaches differ from GravelScape, primarily and fundamentally
in that, using an LEM such as FastScape, the deposition rate is determined dynamically using equation 2. Although it is
250   influenced by the subsidence rate, the deposition rate is not necessarily equal to it, as assumed in past applications of (Fedele
and Paola, 2007)'s approach. Furthermore, in a LEM, the deposition rate and subsequent grain size fining become a function of
not only subsidence rate but also sediment supply and is also likely to be affected by channel dynamics. Comparing our results
to those obtained assuming a single channel where deposition rate is equal to subsidence rate will therefore help illustrate the
effect of autogenic processes on grain size fining.

255   For this comparison and validation, results replicating/relating to past applications will be referred to as SubsidenceGravel1CH
since these methods use subsidence to determine fining rates along a single river channel (1CH) profile. To generate our refer-
ence solution (SubsidenceGravel1CH) we will impose a known subsidence rate as shown in Figure 1, similar to that of Duller
et al. (2010). In our SubsidenceGravel1CH setup, we denote L_m the orogenic or mountain width , u the uniform uplift rate in
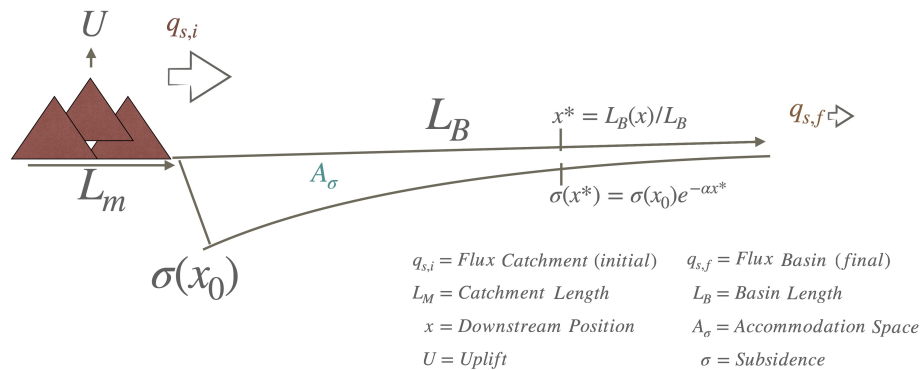
Figure 1. Sample basin set up using Duller et al. (2010) imposed subsidence. All figures within this work will be draining an orogenic front
to the left to an eventual sink to the right even if only results within the basin are shown.

the mountain, and L_B the basin extent. Following Duller et al. (2010), we assume a subsidence rate of an exponential form
260   mimicking the flexural deflection of a foreland basin according to:

$$\sigma(x^*) = \sigma_0 e^{-\alpha x^*} \tag{9}$$

where σ_0 is the subsidence at the orogenic front and α is the dimensionless rate of decay of the subsidence away from the front.
Assuming, as done in Duller et al. (2010), that deposition rate is equal to subsidence rate leads to the following computation of

$y*$ used to calculate SubsidenceGravel1CH grain size fining through 3:

$$y^*(x^*) = (1 - \gamma_p) \int_0^{x^*} \frac{\sigma(x')}{q_s(x^*)} L dx' \tag{10}$$

3.2 Past Applications: Controlling Sediment Infilling/Bypass

There are a number of terms, equations, and parameters from past literature (eg: (Duller et al., 2010) and Whittaker et al., 2011) related to the analysis of grain size relative to basin subsidence and flux that will be used throughout the analysis and discussion of our results. For example, Duller et al. (2010) express the sediment flux at a given downstream point, x^*, as the difference between the initial flux leaving the orogen ($q_{s,i}$) and the downstream integration of the subsidence rate (also referred to as the accommodation space due to subsidence A_σ) according to:

$$q_s(x^*) = q_{s,i} - A_\sigma(x^*) = q_{s,i} - (1 - \gamma_p) L_B \int_0^{x^*} \sigma(x') \, dx' \tag{11}$$

We will also denote $q_{s,f}$ the flux leaving the basin that was not trapped as stratigraphy within the available accommodation space.

Duller et al. (2010) also introduces a parameter F as the ratio of the incoming flux over the integrated deposition rate in the basin (see Figure 2 A-C). F indicates the under, over, or filled state of the basin. For a given subsidence rate $\sigma(x)$, there is therefore a one-to-one relationship between $q_{s,i}$ and F that we can express as:

$$q_{s,i} = F(1 - \gamma_p) L_B \int_0^1 \sigma(x') dx'. \tag{12}$$

When F is larger than 1 there is more incoming flux, $q_{s,i}$, than the basin subsidence can accommodate, A_σ, producing an outflow of sediment from the basin ($q_{s,i} > A_\sigma$ and $q_{s,f} > 0$). In contrast, when F is smaller than 1, the basin is under-filled ($q_{s,i} < A_\sigma$). For the purposes of clarity, when F is less than or equal to 1 we refer to this as an under-filled or limited bypass basin. When F is greater than 1, but less than or equal to 10 we refer to this as a filling or low bypass basin (Figure2 A). When F is greater than 10, the basin is referred to as an over-filled/high bypass state (Figure2B). Duller et al. (2010) has well studied and described the impact of F on grain size (Figure 2 D). Duller et al. (2010) observed that increasing the initial subsidence, increasing the subsidence decay (α), or decreasing the sediment flux all decrease F and increase subsequent grain size fining rates.

Once the system has reached steady-state, i.e., once the flux coming out of the mountain area is equal to $U L_M$, we can derive the following relationship between F, U and σ_0:

$$F = \frac{U L_M \alpha}{\sigma_0 L_B (1 - e^{-\alpha})} \tag{13}$$

In our numerical experiments, we will vary F by varying σ_0 (Figure2C).
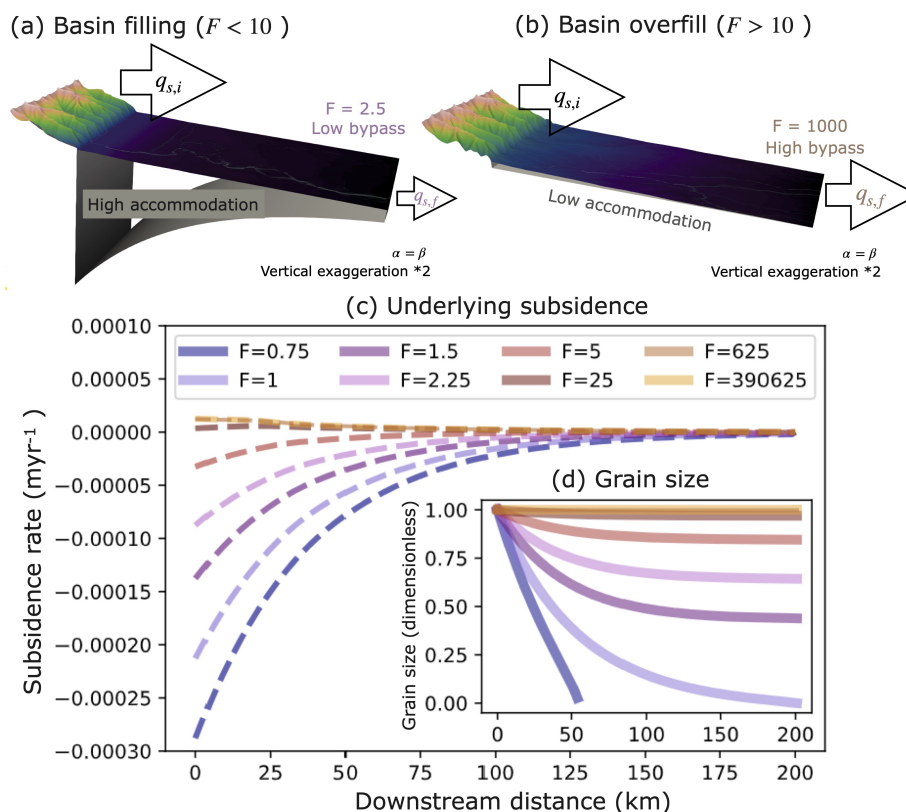
Figure 2. Example imposed subsidence set ups with multi-channels (panels ab) and single channel (panels cd) grain size approaches with changing F through underlying subsidence and a constant incoming flux. The dashed lines show the underlying subsidence for a constant incoming flux used to alter the F ratio whereas the solid lines in the inset plot show the corresponding (SubsidenceGravel1CH) past approaches to grain size fining. Lower F values (eg: blue to pink lines and setup A) in this case have higher subsidence, higher basin capture of sediment, low bypass, and higher grain size fining. High F values (eg: brown lines and set up B) have low underlying subsidence, high bypass leaving the basin, and low grain size fining.

Note, however, that the Duller et al. (2010)'s solution remains constant over time after initial conditions are set, GravelScape numerical simulations are truly time-dependent and can evolve. This means that, from the onset of any experiment, the sediment flux will first increase with time until it reaches a steady-state value given by uL_M. All the results and validation we show correspond to this steady-state situation such that they are directly comparable to Duller et al. (2010)'s solution that assumes
295 a constant incoming sediment flux. Later in the paper we will present model results in which the subsidence is derived from flexure of an assume thin elastic plate for which we will show the complete transient solution. In the flexural results we will compute F using an alternative method of directly computing the flux measured exiting the mountain relative to the integral of the accommodation space.

For the validation, noting that sediment flux is the upstream integral of the deposition/subsidence rate we can substitute
300 Equation (9) into Equation (10), to obtain:

$$y^*(x^*) = -\ln\left(1 - \frac{1 - e^{-\alpha x^*}}{F(1 - e^{-\alpha})}\right) \tag{14}$$

which, in turn, can be used to obtain an analytical expression for the grain size fining curve, which we refer to as the Subsidence­Gravel1CH solution (Figure 2 D) and to which we will compare our numerical solutions.

Contrary to Duller et al. (2010)'s single downstream profile setup where n_y=1, GravelScape is made of n_y grid cells in the
305 across basin direction and n_x cells in the downstream, long profile direction. All grid cells are square and of linear dimension $\frac{L_M + L_B}{n_x}$. However, during the validation step, we will also perform numerical experiments in a pseudo-1D experimental setup, where the number of nodes in the y-direction is set to 2, the smallest permitted in the current implementation of FastScape (Bovy, 2021). With only $n_y = 2$ grid cells, only one single river channel can form. We will label these results as GravelScape1CH, to differentiate them from the results of the full, multi-channel (M number of channels), and $n_y > 2$ model
310 runs, which we will call GravelScape$M$CH. An example of the surface drainage of GravelScape 1CH (2 cells) and GravelScape MCh (>20 cells) is shown in figure A2 E vs G.

Fining solutions will be normalized by the source distribution for all results (such that the grain size at the mountain source will be 1) and the value at the outlet (directly before leaving the basin at base-level) can indicate the total fining that has occurred (see (Figure2D). For example, an outlet grain size of 0.75 indicates that the grain size is 0.75 that of the source or has
315 decreased by 25 percent from the source. Figure2D shows that the majority of the 1CH subsidence induced grain size fining occurs within the first 25-50 (eg: fan dominated) percent of the basin downstream distance from the orogen source. Thus, we can also compare the fining after the first 25 percent of the basin between model runs and already pull out differences, for example, related to subsidence.

In theory, the difference between the GravelScape1CH (theoretically comparable to SubsidenceGravel1CH - see validation
320 for actual comparison) minus GravelScape$M$CH should tell us the impact of multi-channel, varied deposition, autogenic grain size fining across the model opposed to soley single channel, subsidence controlled grain size fining and will be referred to as '1CH-MCH Fining' or 'Autogenic Divergence Fining'. Alternatively, SubsidenceGravel1CH or GravelScape1CH (after validation) can be referred to as 'Subsidence Induced Fining'. Consequently, GravelScape$M$CH would depict the 'Total fining' (autogenic and subsidence induced fining). If there is erosion in the channel, the flux and subsequent grain size would also
325 increase downstream, but this is will not exceed a dimensionless grain size of 1 (cannot be coarser than the input source).

3.3 New LEM Additions: Altering Surface Topography and Fan Extent through Discharge

Another major difference between our LEM-based solutions and SubsidenceGravel1CH is in the computation of surface topography that is inherent to an LEM and excluded in past applications. The topography is likely to exert a strong control on the deposition rate and thus on grain size fining, especially when considering the dynamics of river channels in the basin. In
330 simplifying the system, neither channel dynamics nor surface topography were considered in Duller et al. (2010). So to vali-

date the grain size distributions computed with GravelScape against Duller et al. (2010)'s predictions, we need to consider the controls on topography in the LEM.

As shown by Braun (2022), there exists an analytical solution to the steady-state topography in the basin but only under the assumption that there is no subsidence. Braun (2022) note, however, that the main characteristics of that topography are

335 only mildly affected by subsidence (in reducing topographic height and infilling time). That steady-state solution is made of two parts: close to the mountain front, a first segment characterized by a constant slope is interpreted as a sedimentary fan and connects to a second, curved segment that connects to the base level and is interpreted as an alluvial plain. The size of the fan is controlled by the relative discharge coming from the mountain area compared to the contribution from rainfall in the basin (Braun, 2022). If rainfall in the mountain and in the basin are the same, the fan size is equal to the mountain catchment area

340 feeding the fan. Meanwhile, if the rainfall in the mountain area is greater/smaller than the rainfall in the basin, the size of the fan will be proportionally greater/smaller than the source catchment area. Following Braun (2022) we call L_0 the fan extent (or length) without subsidence and we can write:

$$L_0 = \nu_M L_M / \nu_B \tag{15}$$

where ν_M and ν_B are the rainfall rate in the mountain and basin areas, respectively. To parameterize the effect of the subsidence

345 on the topography (shown in Figure 3, we introduce another dimensionless quantity, β, that is the product of the fan length, L_0, to the length scale of decay of the subsidence rate away from the mountain front, L_B/α:

$$\beta = \frac{\nu_M L_M \alpha}{\nu_B L_B} \tag{16}$$

We see that for values of $\beta < \alpha$, sedimentary processes control the topography (fan extent and height) and the topography is concave (Figure 3A,B1, and C). As β approaches α, the topography transitions from concave to more flat and convex

350 (Figure 3A and B2). Finally, as β becomes much greater than α, the topography becomes flat and linear as the fan size, L_0, becomes larger than the basin width, L_B, and no alluvial plain can develop (Figure 3A). This corresponds to the 'constrained system' as defined in Braun et al. (2023). Since larger β tend to produce flatter topography, they are more prone to form local minima (lakes). Within this study, cases where $\beta < \alpha$ will be referred to as producing a concave topography and cases where $\beta >= \alpha$ as producing a convex topography. We will achieve these variations in β by changing the orogenic zone precipitation

355 rate relative to the downstream basin. Increasing G from a more detachment limited ($G = 0.2$) to transport ($G = 1$) limited scenario alters the topographic profile to become more convex with greater diffusivity (Figure 3A). Note that we display a wide range of β values in Figure 3, however, most basins in the real world display a $\beta < \alpha$ with $\beta >= \alpha$ (Braun et al., 2023) as the exception corresponding to megafans that may have an extent much larger than the flexural wavelength of the underlying elastic lithosphere.

360 In Figure 4, we show how both F and β control the shape of the LEM predicted topography. We see that the topographic height scales non-linearly with F but inversely with β. This is because larger subsidence (smaller, basin filling F values) leads to lower surface topography (Figure 4 blue and pink lines). The larger the fan extent is, compared to the extent of the subsidence (eg: Figure 4 B and C), the further and more equally distributed are the sediments across the model producing a relatively flat topography. Notice that the underlying subsidence across all comparable F values is the same regardless of β.
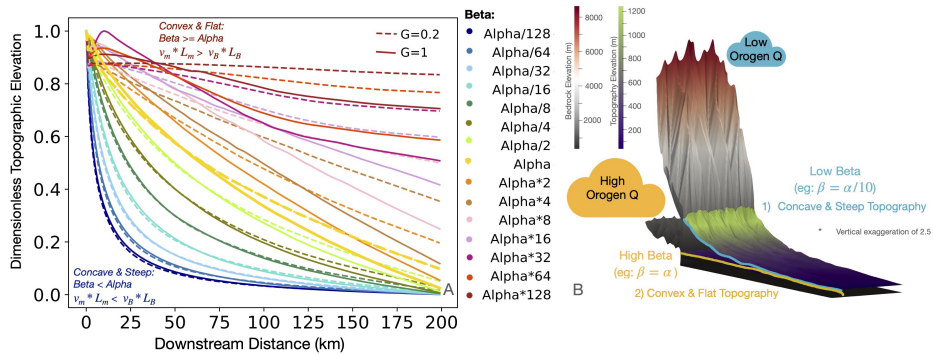
Figure 3. Example model set ups of basin/fan topography with a changing β (Eq. 16) through v_m (orogen precipitation) at steady-state with a constant flux and constant, low underlying subsidence rate. We can see when β is less than (green to blue) α (subsidence decay), the basin long profile is concave, the fan slope is much steeper, and their is a clearer fan (orogen dominated) to basin transition. When β is greater or equal to α (yellow to red), the basin long profile is linear or convex, the fan slope is minimal, and the orogen discharge dominated fan extends over the entire basin. In the line style (G=0.2 is dashed and G=1 is solid), we show the impact of decreasing the sediment transport coefficient G, whereby a lower G produces a flatter topography (especially with a high β). Panel A shows the across basin, steady-state average topographic profiles of different β set ups and panel B shows the output of two contrasting β's for the final steady-state time step.
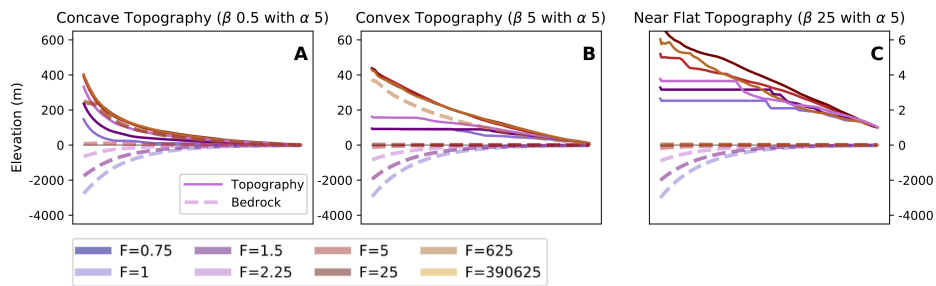
Figure 4. Example of the topography (solid lines) under differing underlying bedrock (dashed lines) subsidence(related F shown in colours purple to brown) and under three β set-up (convex ($\beta = \alpha/10$, concave ($\beta=\alpha$), and near flat ($\beta> \alpha$) topograpghy) in panels A-C respectively. All figures were made with a constant incoming sediment flux, K, and G.

3.4 New LEM Additions: Internal (Autogenic) Dynamics

In Figures 13-A1, we show snapshots of results from the LEM, with sufficient number of grid cells, n_y, to allow for multi-channel dynamics and after steady-state has been reached, depicting variations in deposition, topography, drainage dynamics and recovery time within the model in space (x and y) and time/depth (z) that would not have been accounted for in past applications of the grain size self-similar model but can (and will later be analyzed) impact GravelScape. Since external

370 forcings (e.g., the imposed subsidence/uplift and the spatial variations in rainfall rate) are held constant at steady-state, we will refer to these processes/variations as 'autogenic' or 'internal dynamics' , induced in a wide enough basin to allow for multi-channel dynamics.

3.4.1 Autogenic Dynamics: Depositional Divergence and Topographic Variation

At steady-state, erosion and deposition (dh/dt) should theoretically be equivalent to underlying uplift and subsidence condi-
375 tions. This is generally true. However, shown in Figure 13, deviations in deposition rate appear as $\overline{dh/dt}$ oscillations around the subsidence curve, when averaged across the basin (n_y) and over steady-state time steps.
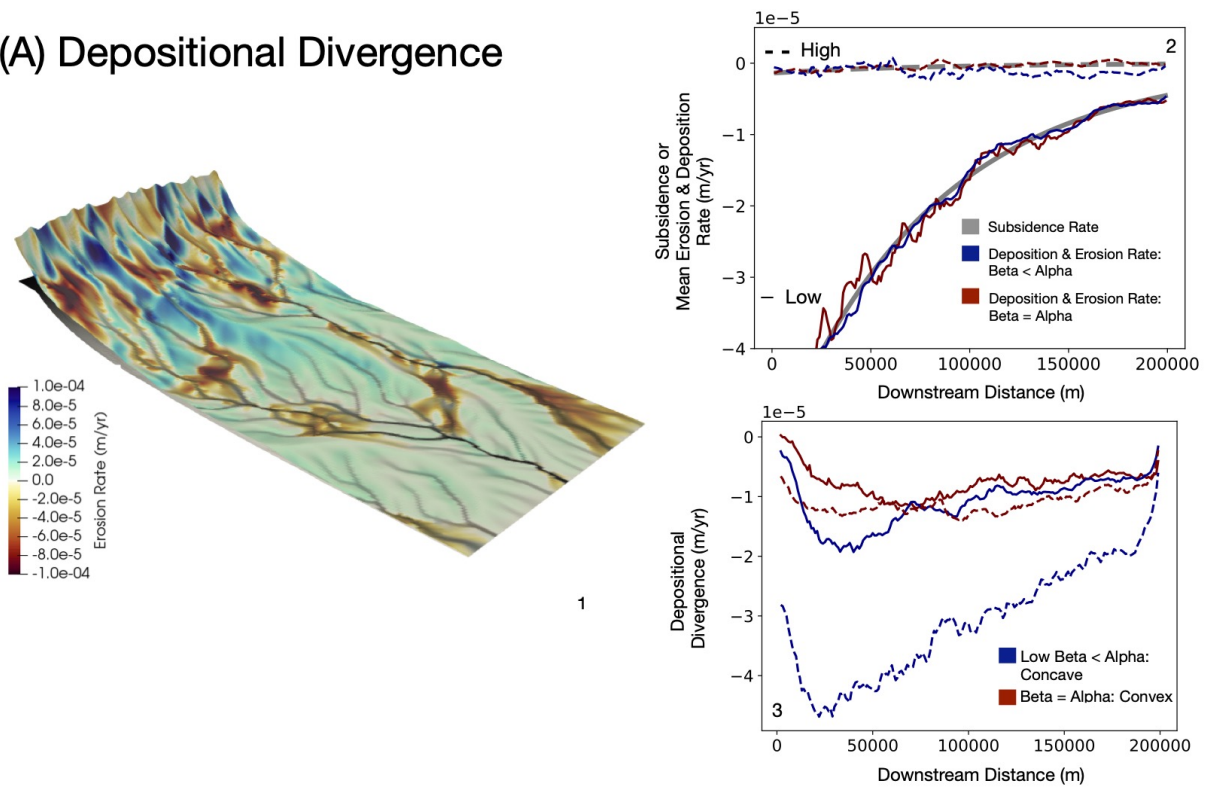
Figure 5. Example of the variation in erosion (blue) and deposition (negative values in red) rate across the basin for a given steady-state time step (A1). A2 shows the across basin and multi-steady state time step average erosion and deposition rate around the mean subsidence rate. A3 highlights the oscillations in deposition/erosion by removing the underlying mean subsidence trend. In A2 and A3, the dashed lines depict a high F basin set up (low underlying subsidence) and the solid lines have a high subsidence (low F). The red values depict the results of a set-up with a convex topography through a high upstream discharge β and the blue lines show a concave long profile with a low upstream β discharge. The highest variation in deposition and erosion rate across the basin and over time occurs with a concave topography with low β and a low subsidence with a high F (dashed blue line).

The greater the amplitude of the oscillations, the greater the variations in deposition/incision across the model and over time (Figure 13 A2). Shown in Figure 13 A3, the magnitude of these oscillations in $\overline{dh/dt}$ relative to subsidence rates can be better illustrated by subtracting from the sedimentation rate the imposed subsidence rate to obtain what we will call the 'depositional

380   divergence rate' (τ):

$$\tau = \overline{[dh/dt < 0]} - \overline{\sigma} \qquad (17)$$

We see that the depositional divergence rate increases with reduced subsidence rate (or increase F values) (Figure 13 A3 solid vs dashed lines) and increases with reduced upstream discharge (or decreasing β) (Figure 13 A3 blue vs red lines). Variations in deposition and erosion rate across the model lead to local infilling and erosion in the topography over time and space that

385   we will describe in terms of depositional waves and rugosity respectively.

We see that, far from being uniform, sedimentation appears to take place in pulses or waves that propagate through the sedimentary basin in the x-direction (through oscillations of infilling and incising between base level and the mountain source or vice versa) and also cause variation in local infilling and incision across the basin, i.e., in the y-direction (Figure 6). For a video of the depositional waves filling a fan long profile over time, please see the supplementary materials.

390   Looking at successive time steps and depending on the local profile accommodation space in Figure 6, depositional waves can even be regarded as the depositional equivalent of erosional knickpoints in that they initiate at base level and then backfill channels in an upstream direction gradually raising the entire river profile. Similar depositional features have been evidenced by (Carretier et al., 2020). Depositional waves retrogradation and progradation have also been described in the real world (using a range of terms) especially in deltas and plains (eg: (Stouthamer and Berendsen, 2007; Edmonds et al., 2022; Nicholas

395   and Quine, 2007; Clarke et al., 2010)) irrespective of an external forcing event. Sedimentation waves are driven by cycles of deposition/erosion in the sedimentary system and this generates variation and local accommodation space along the basin long profile. Cycles of deposition/erosion can also lead to further variation in topography across the basin (rugosity μ) and channel avulsion (ω).

We define the rugosity (Figure 7) as the standard deviation of the topography across the basin (i.e., the y-direction). In

400   other words, it is the average difference between the interfluves and fluvial channels. The rugosity is also the thickness of the sediment layer that is the most active and will be reworked (incised and infilled) over multiple steady-state time steps. Only a portion (in time and space) of this layer is preserved.

3.4.2 Autogenic Dynamics: Drainage Routing

Channel mobility (Figure 8) is a generalized term that encompasses any process that causes changes in the channel geometry

405   across the basin, i.e., channel avulsions, meanders, migrations, divergence, lakes, etc. For a video of the movement of channels within the basin, please consult the supplementary materials. We define the mobility frequency parameter, ω, as the sum over all time steps (or a sub-ensemble of time steps) of the number of locations along the main channel that are not part of the main channel at the next time step (or vice versa) divided by the number of time steps. Determining parameters ω and ζ requires first to compute, for each point in the x-direction, the location of the maximum discharge along the y-direction. We will refer
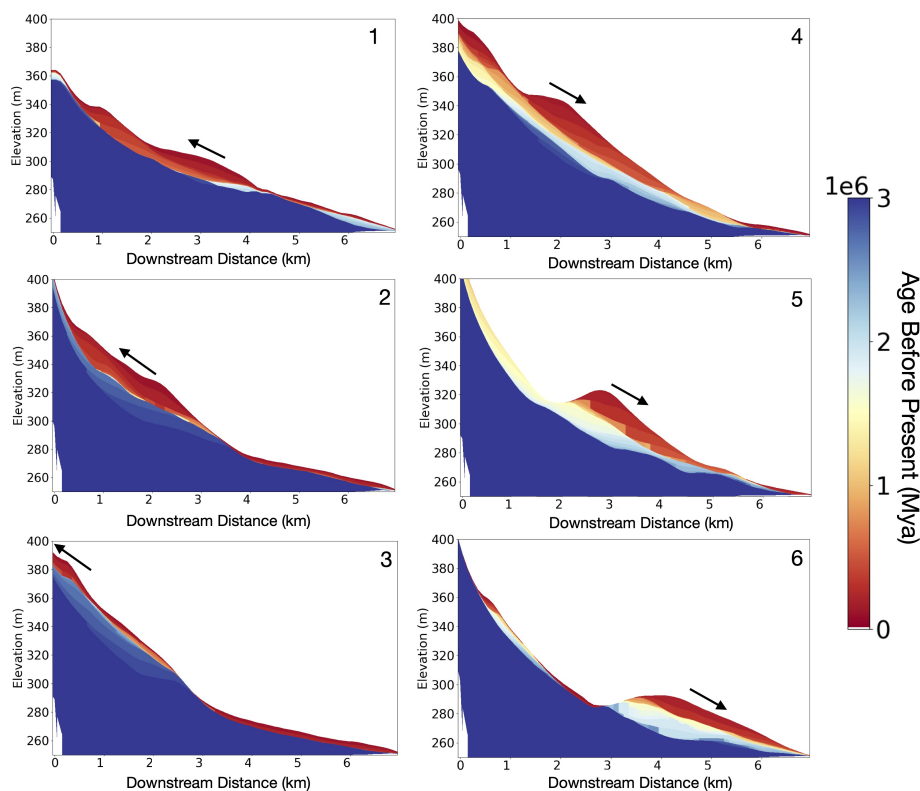
Figure 6. Follow panels 1-6 to show the propagation of a depositional pulse up or downstream along a basin long profile. Red depicts a recent deposit and blue is a deposit that occurred greater than 3 Mya from the red surface deposition. To see a video of depositional waves, see the supplementary materials.

410   to this as the 'main channel'. Alternatively, we can identified all 'major channel pathways' using the geometric mean (over time and across the basin) for the lowest discharge solution (out off all simulations run) as a threshold that evolves downstream (capturing how discharge naturally increases downstream within river systems). Both methods produced comparable results, but the 'main channel' method is more discharge independent for ω and ζ computation, while the 'major channel pathways' method is useful to identify channel vs. floodplain areas within stratigraphic profiles. The D_x grain size depositional areas for

415   a given time step often matched very closely to the geometric mean 'major channel pathways'.

     Local minima (ζ) are a topographic phenomena that form in flat topography (Figure A1.2) or in a basin with topography below base level (Figure A1.1). The resulting closed depressions need to be resolved because they disrupt the flow routing and cause hydraulically unrealistic results in discharge computation (Cordonnier et al., 2019) that can impact deposition and subsequently GravelScape (see validation). Local minima have also been referred to as pits or flat bottom deposits (Lindsay,

420   2016) or, once filled, as lakes. In FastScape, the algorithm developed by Cordonnier et al. (2019) is used to resolve the local
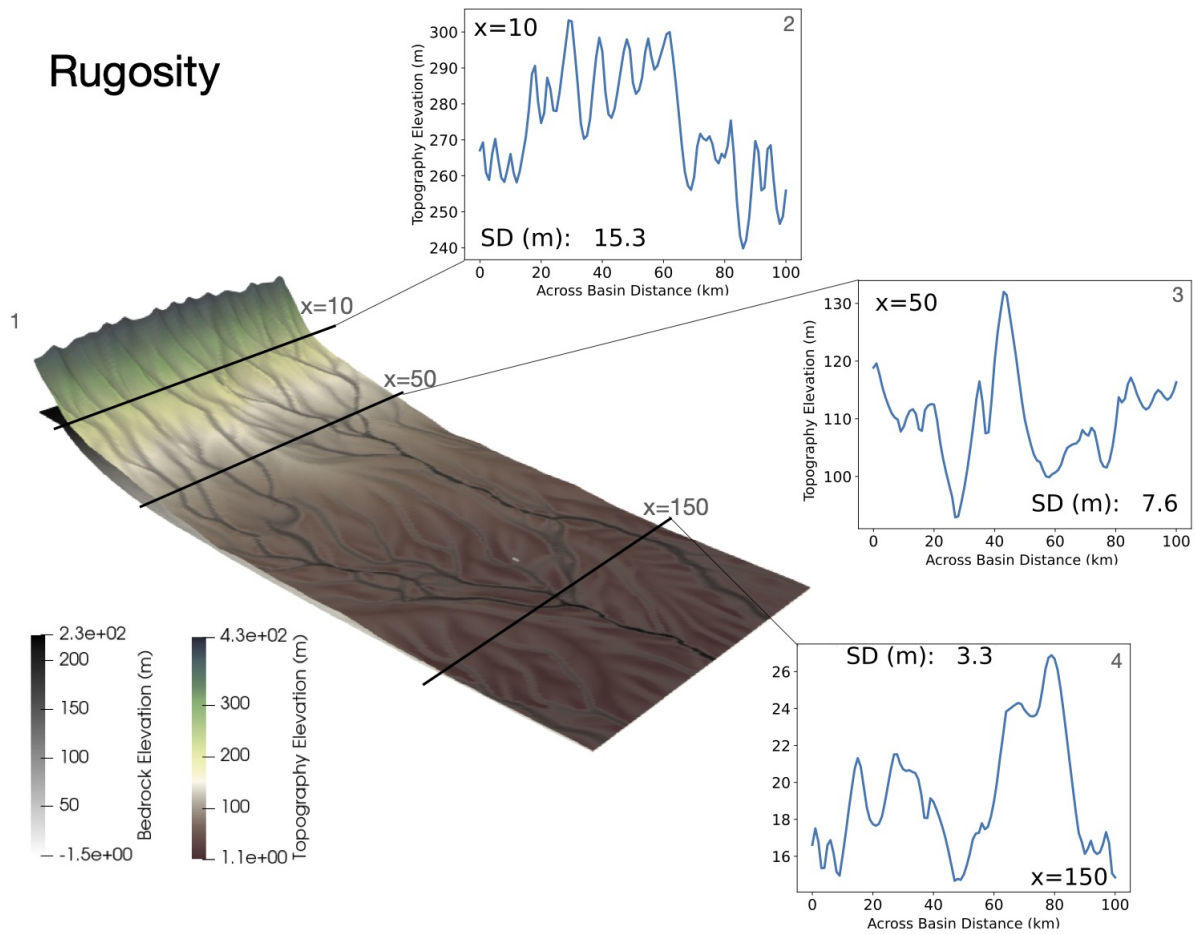
Figure 7. Example of the variation in topographic height at varied downstream locations (eg: 10km in subset 2, 50km downstream in subset 3, and 150km in subset 4). The entire basin has a constant underlying subsidence and external set up, yet expresses across basin variation.

minima. This algorithm finds, for every local minima, the sill or exit point of the corresponding depression to form 'lakes' and then connects the various depressions or lakes to determine a flow path towards the model boundaries or base level.

Even resolved local minima can still be problematic for our grain size computation because when a local minima is encountered, Yuan et al. (2019)'s algorithm to solve equation (2) cannot be used and sediment is simply dumped uniformly into the corresponding lake and no grain size can be accurately computed. Once the minima is filled, the solution moves to complete bypass across the lake/depression. In order to assess how dominant local minima are for any given numerical experiments, we compute the number of local minima in the main channel over N time steps and transform it into a frequency, ζ, by dividing the result by $N-1$. In this way, we can assess if we are analyzing a scenario where discharge and drainage is heavily influenced
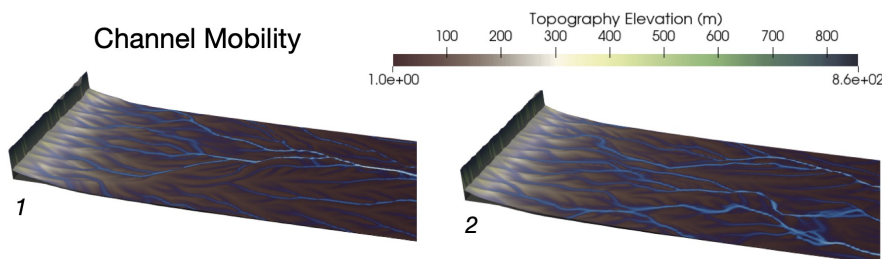
Figure 8. An example of channel reorganization over two different time steps within the model. To see a video of these images, consult the supplementary materials.
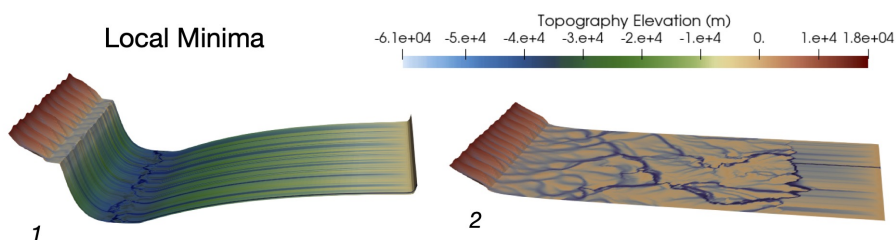
Figure 9. An example of local minima forming in negative topography from a rapidly subsiding basin (subset 1) or in very flat topography (eg: within the outer reaches of the basin in subset 2).

by local minima or if it is a 'normal' fluvial routing. To see when local minima are most prevalent across values of F, G, and β refer to A1. Generally, deceasing K or increasing G can reduce the local minima unless the basin is strongly underfilled (negative elevation), but we often compared solutions with a constant K or G and thus, need a way to flag minima dominated scenarios.

3.4.3 Autogenic Recovery Time υ

Using the rugosity divided by the depositional divergence, we can derive an autogenic recovery time (υ):

$$\upsilon = \frac{\mu}{\tau} \tag{18}$$

In theory, the autogenic recovery time is the time it would take to incise or infill the amount of variation in topography (rugosity) induced under the same imposed subsidence rate (ie: driven by the depositional divergence rate). This recovery time will be discussed in further detail during the validation.

3.5 Set-Up: LEM Input Parameters

440   In Table 1, we give the value of the LEM parameters, including the spatial and temporal resolutions, and the parameters that have values common to all model experiments.

Symbol	Value	Description
n_y	$[2(1CH) vs 101(MCH)]$	Number across model cells (including orogen and basin (min.20 n_y cells for multi-channel functionality)).
n_x	$[202 - 251(FSubs); 251(FLX)]$	Number down model cells (including orogen and basin (min. approx. 40 cells for multi-channel functionality)).
$Cellsize$	$[100 - 2000(Sup.); 1000(all)]$	Size (m) of a grid cell with 1000m as the reference case.
L_m	$[1e3 - 50e3(FSubs); 50e3(FLX)]$	Total Mountain length/downstream (x) distance (m).
L_B	$[40e3[Sup.] - 200e3(all)]$	Total basin length/downstream (x) distance (m).
$Timestep$	$[500 - 10000(Sup.); 10000(FSubs); 1000(FLX)]$	Time step between model outputs (yrs).
$Totaltime$	$[25e6 - 20e6(all)]$	Total simulation run time (yrs).
$Steadytime$	$[1 - 5e6(all)]$	Final steady-state years of the model that were analysed or averaged (yrs).
m	$[0.4(all)]$	SPL Area exponent
n	$[1(all)]$	SPL Slope exponent
G	$[0.2 - 1(FSubs); 1(FLX)]$	Depositional dimensionless parameter. One is the reference value.
K	$[7.5e - 6 to 7.5e - 5(FSubs); 7.5e - 5(FLX)]$	SPL erodiblity K that was kept constant between the basin and orogenic area.
U	$[1e - 2(all); 1e - 2 - 1e - 4(Sup.)]$	Uplift Rate (m/yr)
$alpha$	$[2.5 - 5(FSubs); 5(FLX)]$	Imposed Subsidence decay rate.
F	$[10000 - 1(all)]$	Bypass Ratio: Incoming orogenic flux relative to basin accommodation.
σ_0	$[-2.7e - 4 to - 2.7e - 8(FSubs)]$	the initial subsidence after leaving the orogenic front (FSubs only).
β	$[alpha/1000 - alpha * 1000(FSubs)]$	(we tested a range of values).
v_m	$[0.004 - 200000(FSubs); 0.8(FLX); 20(FLXSup.)]$	Precipitation falling on the orogen (range of values).
v_B	$[1(all)]$	Precipitation falling in the basin.
I	$[250 - 0(all)]$	Initial topography gradient of 250m (mountains) to 0m (base-level).
$Diff_B$	$[0.03 (FLX); 0.1 (FSubs)]$	Bedrock diffusivity.
$Diff_S$	$[0.1(all)]$	Soil diffusivity.
$Porosity$	$[0(all)]$	Sediment porosity
$\overline{D_0}$	$[1(all)]$	D50 grain size leaving the orogen source.
ϕ_0	$[0.75(all); 1 - 0.5(sup.)]$	Standard deviation of the source distribution.
C_v	$[0.75(all); 1 - 0.5(sup.)]$	Grain size coefficient of variation.
C_1	$[0.75(all)]$	Constant of the downstream decay of the grain size standard deviation.
ρ_L	$[2800(FLX)]$	Lithospheric rock density.
ρ_A	$[3200(FLX)]$	Asthenospheric rock density.
E_T	$[20e3(FLX)]$	Effective elastic plate thickness

Table 1. GravelScape inputs for all supplementary or appendix (Sup.), imposed subsidence scenarios to generate a given F (FSubs.), single channel (1CH), multi-channel (MCH), and flexural (FLX) model scenarios. The flexural model example is multi-channel and attempts to replicate a set-up realistic/common within the real-world. The imposed subsidence scenarios are single or multi-channel during the validation and are more theoretical to generate a given F even with the subsidence is unrealistic for the mountain size.

4   Results

4.1   Presenting GravelScape

In Figure 10, we show computed topography, erosion/deposition rate, drainage, grain size distribution over time (D_t), and

445   grain size at a instantaneous time step (D_x) for a reference model experiment at a series of arbitrary consecutive time steps.
We used $F = 10000$, $\beta = \alpha/10$, and $G = 1$. Even though the model has reached a quasi steady-state, important fluctuations
in topography, discharge and grain size take place in response to what appears as large avulsions. We note that, on average,
the grain size tends to decrease from the mountain front to the base level. We also note that the predicted grain size is coarser
in channels (regions of high discharge) and is highly variable spatially and temporally. This implies that the predicted grain

450   size in the channels should be used to compare our model's predictions to the predictions of Duller et al. (2010)'s model that
is limited to a single or amalgamated channel body. The strong variability in space and time also implies that the grain size
predictions must be averaged over many time steps (eg: >10Kyr) for comparison with Duller et al. (2010)'s model that assume
that deposition rate is equal to subsidence rate and is thus a very smooth function of x and t. Interestingly, the variability in
mean grain size predicted by our model appears to be similar to the variability observed in many natural settings. We also note

455   that there is a small, yet non-negligible, grain size fining in the mountain area, such that the mean grain size of the material
leaving the mountain front is not exactly at a value of unity, corresponding to the assumed grain size at the source.
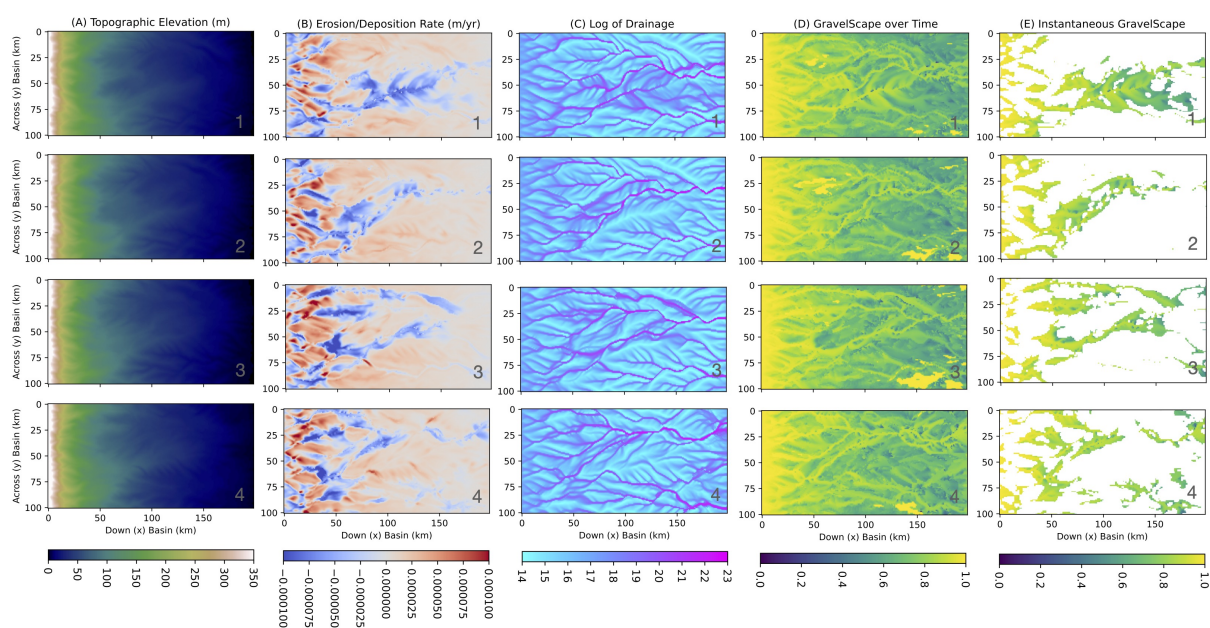
Figure 10. Four steady-state outputs of the plan view surface of A)Topography, B) Erosion/deposition rate, C) Log of drainage, D) GravelScape over time (D_t), and E) instantaneous GravelScape (D_x) for 1-4 given time steps. Please note in B that where the solution is negative, there is deposition (blue) and where positive there is erosion (red).

In Figure 11 (and supplmentary video) we show how grain size computations at every successive time step can be used to reconstruct a complete grain size stratigraphic record. In panel A, we show the 3D geometry of the system as well as computed surface grain size, D_t, and deposited grain size, D_x, as contours over the surface topography. In panel C we show a vertical
460   profile along the x-axis of the predicted grain size. We see that the general trend of grain size fining from mountain front to base level has persisted throughout the model history but has also been punctuated by episode of reduced (coarse grain size deposited away from the mountain front) or enhanced (all coarse grains deposited in the proximal fan area) fining. In panels D and E, we show vertical cross-sections in the y-directions at two x-locations as indicated in panel A. As expected, the mean grain size is greater in the proximal section (panel D) than in the distal one (panel E) but both sections display relatively large
465   variability produced by the presence of paleo-channels containing coarser grains. From these diagrams we can estimate the life span of these channels and the corresponding interfluves.
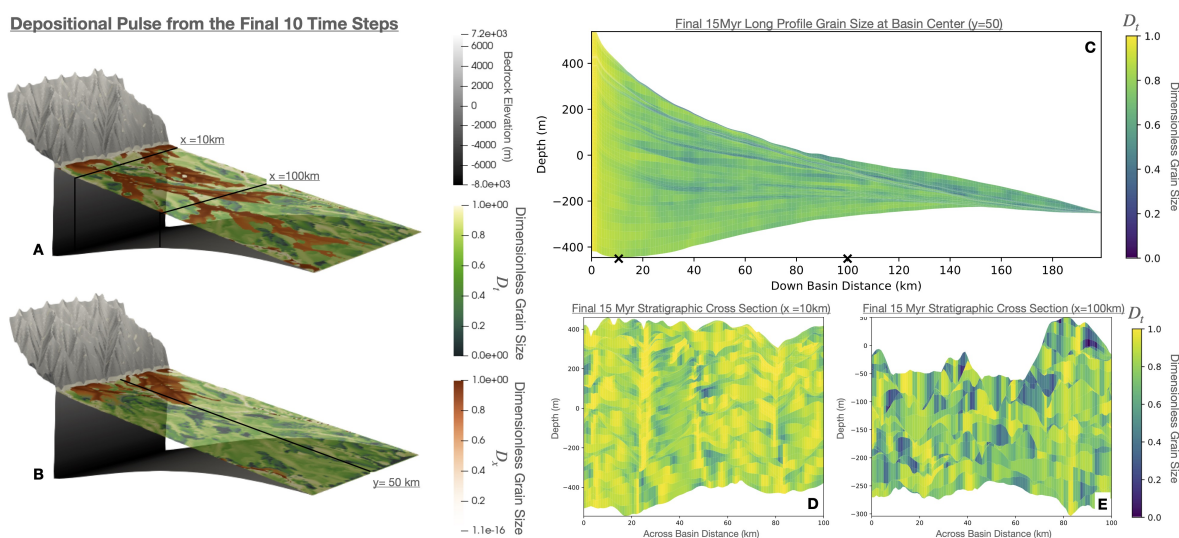
Figure 11. Introducing GravelScape using an adaptation of (Fedele and Paola, 2007)'s self-similar grain size model into FastScape's sediment model with multi-flow routing and multi-channel dynamics. Figure A and B are the orthogonal view outputs from the final steady-state outputs of the model. The grain size deposited at a given time step (D_x) is shown in orange, on top of the subsequent grain size deposits from previous time steps (D_t) that are still exposed at the surface and shown in green (fine gravel) to yellow (coarse). Figure C depicts the grain size deposited over time (D_t) within a longitudinal (downstream preserving x) depth profile as if we were to cut the Figure B straight down the center at y=50km. Figures D and E are stratigraphic cuts across the model (preserving y) shown on figure A at downstream positions x=10km and x=100km. Model stratigraphy will also be presented later in the paper in a similar manner. To see a video of the grain size over time and instantaneous grain size please consult the supplementary videos.

4.2 Initial Single vs Multi-Channel Grain Size Validation

In Figure 12 we display the computed topography, subsidence, and grain size for both GravelScape1CH and the main channel of GravelScape$M$CH as a function of downstream distance (x). The aim of this validation is to determine where GravelScape is able to reproduce or substantially deviates from SubsidenceGravel1CH results that are based on the assumption of subsidence controlled deposition within a single channel without topography. For this validation, we are comparing simulations with an imposed subsidence and simplified, steady-state orogen as depicted in Figure 1.
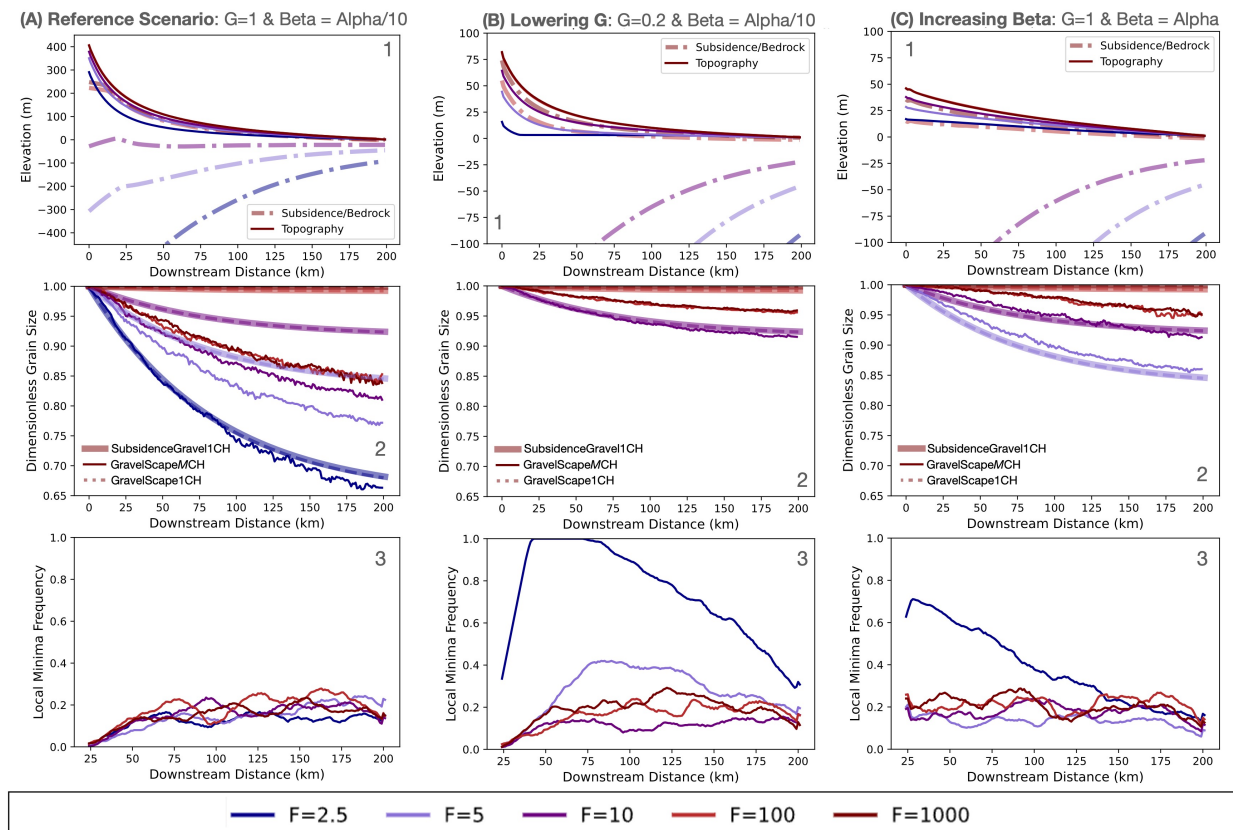
Figure 12. Panels A1-3 depict the reference scenario with a $G = 1$, concave topography (low upstream discharge β) with varying underling subsidence F values (blue to brown). Subset images 1 show the steady-state average basin topography (solid) and underlying bedrock subsidence (dash-dot). Subsets labelled 2 show the grain size fining from the SubsidenceGravel1CH (thickets lines with opacity), GravelScape1CH (dashed lines) (1D), and GravelScape$M$CH (thin and solid lines) (2D) solutions. Subset images 3 show the frequency of local minima occurring within the basin and we will only display solutions with comparable (low) local minima under 0.3. For comparison to the reference solution, panels B1-3 show the same topography, grain size, and local minima plots with a lower G and panels C1-3 show the results with a higher upstream discharge β producing a lower slope.

We see that the GravelScape$M$CH grain size predictions are in good agreement with SubsidenceGravel1CH but produce greater fining under higher F values (Figures 12 A-C panel 2). In other words, across all basin geometries, topographies, and G
475 values (Figures 12 2nd panels), under high bypass (high F shown in red), more rapid fining is produced with GravelScape$M$CH compared to the SubsidenceGravel1CH and GravelScape1CH solutions. Increasing F to high bypass values (red values in Figures 12 2nd panel) within the GravelScape$M$CH solutions eventually converges to a comparable channel mobility frequency and grain size fining rate. When comparing high F scenarios, the deviation of GravelScape$M$CH from Subsidence-Gravel1CH/GravelScape1CH is greatest under the more concave topography (changing β) and with more transport limited
480 (high G) solutions. This appears to show that high bypass, low β, and high G promote the strongest autogenic multi-channel fining and will be investigated more thoroughly in the sections to follow.

Note that, as explained earlier, when sedimentation patterns are dominated by the presence of local minima, the GravelScape algorithm breaks down. For this reason, we did not use model results that are characterized by ζ values larger than 0.3 in our comparison with SubsidenceGravel1CH results. Refer to A1 to see when local minima are most dominant within the model
485 and the supplementary materials shows a similar figure to Fig. 12 including the unrealistic grain size results with high minima for completeness.

4.3 Combined Impact of F, β, G and K on Grain Size Trends

We now investigate how variations in the principal model parameters, namely F, β, G and K affect the distribution in grain size and, in particular, how different they are from the predictions of the 1D, subsidence-driven predictions of Duller et al. (2010),
490 namely SubsidenceGravel1CH. For this we compute the grain size deviation as the difference between SubsidenceGravel1CH and GravelScape$M$CH predicted grain sizes at the outlet (base level) of the model in the main channel. In Figure 13, we show how this deviation as a function of three parameters, namely the depositional deviation (panel A), the rugosity (panel B) and the fan topographic elevation (panel C) for many model experiments in which F, β, G and K are systematically varied. We see that the grain size deviation correlates with all three factors but that the best correlation (first order) is with
495 the depositional deviation, demonstrating that the deviation in grain size fining prediction from the SubsidenceGravel1CH arises from local deviations in deposition rate from the subsidence rate. Rugosity (second order) and topographic height (third order) also tend to occur with higher depositional deviation. However, raising topographic height can also occur in a single channel (2 cell model) without causing any deviation and is thus, it is a step removed in correlation provided that multi-channel conditions are met. Rugosity and especially topography are also more sensitivity to changing K (green), and even β, than
500 depositional deviation causing additional scatter within the correlation whereby decreasing K (green) caused greater rugosity and fan elevations without further increasing depositional and grain size deviation. We can describe the correlations of the three parameters as follows: raising topographic height (third order) promotes increased rugosity (second order) and this increases local infilling and incision (first order) allowing for a deviation in grain size from the mean underlying subsidence.

Inspecting in more detail Figure 13A, we note that the depositional divergence and autogenic induced grain size fining
505 are highest (Fining greater than 0.05) in combined conditions of (1) transport limited solutions (G=1), (2) high (around $F >= 4$) bypass with low underlying subsidence, and with (3) steep/concave topography ($\beta < \alpha$). On the contrary, all $G = 0.2$
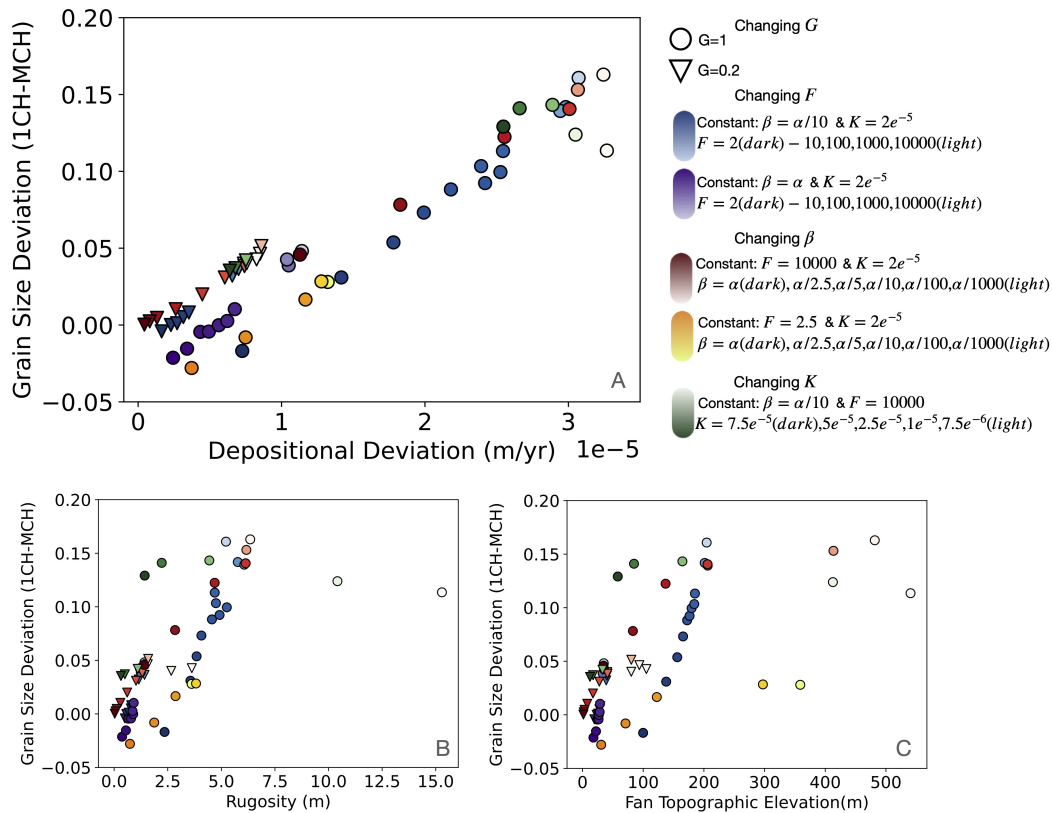
Figure 13. LEM dynamics ((a) depositional divergence (first order), (b) rugosity (second order), and (c) fan topographic height (third order) that have similar correlation trends to 1Ch - MCH grain size divergence across all values of F (blue and purple gradients) , β (brown and yellow gradients), G (circles vs triangles), and K (green gradients). Positive values of grain size deviation indicate greater fining rates than the single channel solutions (SubsidenceGravel1CH or GravelScape1CH). Values (eg: grain size deviation) in panels a-c from different model set ups of F, G, β, and K were average/computed over steady-state, across the basin, and downstream to produce one average value for each set-up.

detachment-limited (triangles), convex (purples) topographies ($\beta >= \alpha$), and low F (yellow) (eg: $F<2$) solutions show insignificant (under 0.05 dimensionless grain size) grain size deviations and, thus, minor autogenic induced grain size fining. Although changing K slightly alters depositional deviation, the resulting grain size fining deviations are all within 0.05 dimensionless unit of one another indicating a insignificant/to very minor control of K on grain size fining deviation.

510

Shown in Figure 14, total grain size fining with multi-channels (captured by the dimensionless grain size at the basin outlet) is correlated with the mean deposition and erosion rate (first order), autogenic recover time (second order), and channel mobility

frequency (third order). Focusing on Figure 14A, we see that the highest total fining occurred (as past applications would predict) under high accommodation (lower F), but the final value for a given F varied between 0.1-0.2 dimensionless grain size depending on β or G. This will be explored further within the discussion.
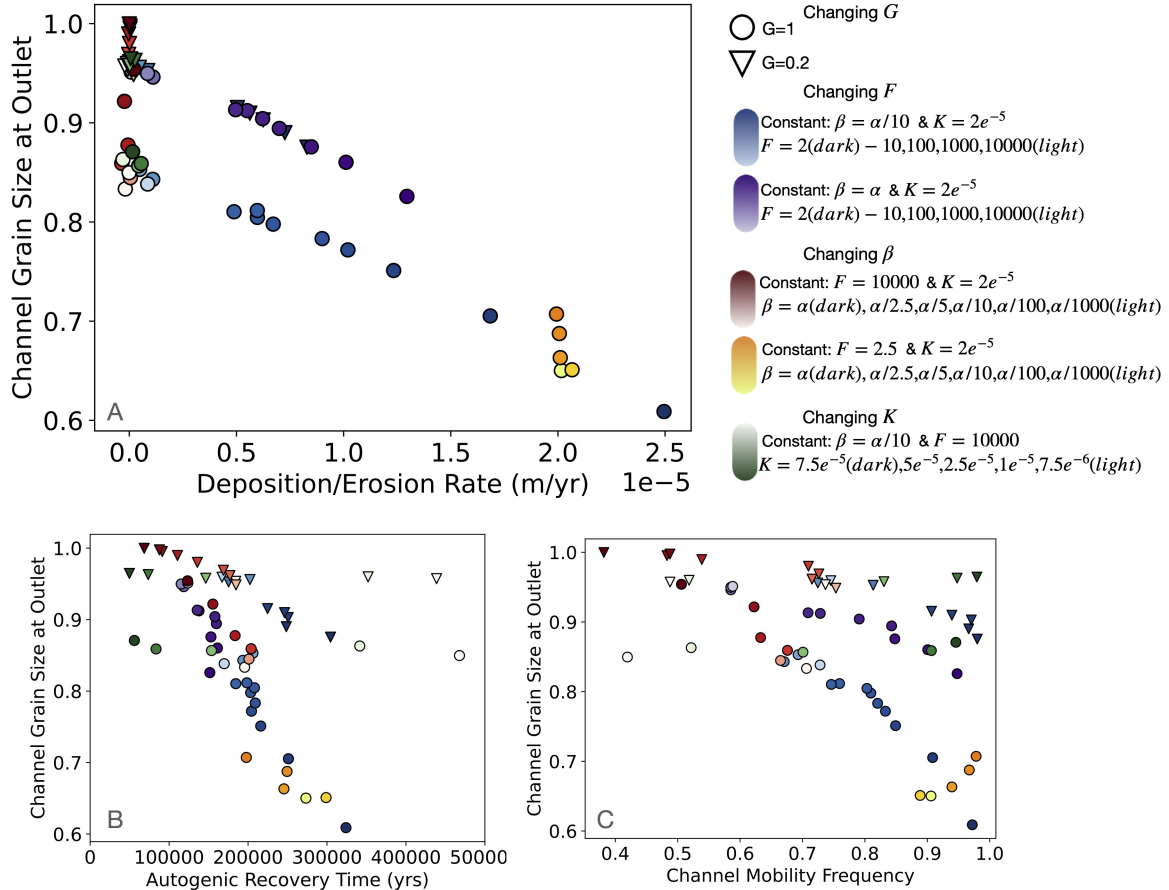
Figure 14. LEM dynamics ((a) mean deposition and erosion rate, (b) autogenic recovery time, and (c) channel mobility) that have similar correlation trends to total M grain size at the outlet (after fining with a source value of 1) across all values of F (blue and purple gradients), β (brown and yellow gradients), G (circles vs triangles), and K (green gradients). Values (eg: channel mobility) in panels a-c from different model set ups of F, G, β, and K were average/computed over steady-state, across the basin, and downstream to produce one average value for each set-up.

Varying the incoming sedimentary flux (or uplift rate in the mountain area) does not change the behaviour of the grain size deviation or total fining as a function of the depositional divergence either, if the depositional divergence or mean deposition/erosion rate is normalized by the sedimentary flux (see Supplementary Materials). Our simulations above used a constant flux, but future analysis (not at steady-state or comparing areas/uplifts) should normalize by the flux when assessing depo-

520   sitional divergence. Varying other, additional parameters, such as C_V or S_D, do not impact the behaviour of the grain size
deviation as a function of the depositional divergence (see Supplementary Materials). Also in Supplementary Materials, we
show similar results obtained by assessing grain size fining fining and autogenic model parameters under changing F and β
with downstream distance (i.e., in the x direction) preserved while averaging or selecting the main channel in the y-direction.
In all the supplementary material figures, the conclusions about the model behaviour are identical to Figure 13.

525   In summary, the greatest variations in grain size deviation (between 0.2 dimensionless units) occur when varying F (blue
circles) in a concave (low β) and transport-limited set-up (high G). This is followed by varying β (red circles) under high
bypass (high F) and transport limited conditions (high G). Total fining is also impacted by the addition of internal dynamics
shifting the final grain size leaving the basin for a given F depending on the G transport or β topography autogenic dynamics.

4.4   Spatial and Temporal Dynamics

530   We performed a large number of simulations with varying spatial and temporal resolutions and show a summary of a few of
these results in Fig. A2. We found that, in all cases with limited local minima ($\zeta < 0.3$), the GravelScape1CH solution matched
the fining trend of the SubsidenceGravel1CH solution when averaged over steady-state. We also found that GravelScape$M$CH
results under low bypass (F=1.25) did not vary by more than a few percent when varying the spatial or temporal resolutions
regardless of the values of G, β, and F (Fig A2). When we increased F (eg: $F => 5$), the GravelScape$M$CH results started to
535   show a stronger dependence on spatial and temporal resolutions in the outer portions of the basin, i.e., near the base level (Fig
A2). This is because high F scenarios show the greatest autogenic influence and, thus, changing the grid and temporal resolu-
tion alter the number of channels and their relative mobility. For further analysis of the impact of changing temporal resolution
on the autogenic parameters within the model please see the supplementary materials. For example, we also experimented with
changing β with different temporal resolutions and found comparable trends and magnitudes within the autogenic parameters
540   aside from grain size (see supplementary materials).

Keep in mind, however, that for the assumption of self-similarity to hold, variability in flow must be averaged over time
scales such that local fine scale hydraulic details collapse. It is therefore not appropriate to consider our model predictions and
especially those relating to autogenic processes on short time scales (i.e., under or around a few hundreds of years). Shown in
fig. A3, the interval under which autogenic grain size fining is averaged can also change the variation around the mean results.
545   However, the mean trends remain the same when averaged, as a guideline, over half an order of magnitude of the autogenic
recovery time or, more generally put, over a window of a few sediment pulses of deposition/incision. See figure A3 for a
comparison of the mean (remains constant) and variation (varies) in grain size across the basin over different averaging time
periods (eg: 1.5 vs 15 Myrs). Averaging over a window ensures that enough potential channel mobility events and depositional
waves can cover the entire basin with sediment. Since the deposition rate varies locally, spatially, and with time at a given
550   magnitude and frequency around the underlying subsidence, it was the objective of this research to analyze the mean autogenic
deviation trend and not a given instantaneous coarser or finer deposition event that may not propagate fully through the basin.

To address this resolution dependence within the high bypass/highly autogenic scenarios, we have implemented three ap-
proaches. Firstly, downstream predicted grain size values within +/- 5 % of the source (orogen) input grain size (eg: within

+/-0.05 dimensionless grain size with a source of 1) can be considered negligible or within the natural spatial/temporal vari-

555 ability of the model (eg: maximum grain size variability range of spatial and temporal resolution within the F>5 scenarios). Secondly, all our results and discussion figures will use the same spatial and temporal resolutions to improve comparison. Next, we implement and recommend that the time step at minimum to be one order of magnitude smaller than the mean autogenic recovery time (50-500kyr in our results) in order to properly capture channel mobility and autogenic reworking. Furthermore, if one wishes to properly represents relevant autogenic processes such as channel avulsions, the time step should be roughly

560 smaller than the average period between two natural avulsions. For larger river systems, such as the Rhine-Meuse, Stouthamer and Berendsen (2007) have suggested avulsion rates at 1-100kyrs scales. Thus, to satisfy the magnitude smaller than the mean autogenic recovery time condition, we used a time step between 1-10 Kyrs. Grid size was chosen to be approximately proportional to the width of a large, dominant channel branch (eg:100-1000m range). This provides reasonable upper and lower bounds for time and spatial stepping in GravelScape.

565 ## 4.5   What controls the autogenic recovery time υ

As shown in Figure 15, the main parameter controlling the value of the autogenic recovery time (rugosity divided by the depositional divergence), υ, is the erodibility parameter, K. Increasing K by an order of magnitude (i.e., from 7.5×10^{-6} to 7.5×10^{-5}) results in a decrease over a similar range for υ (i.e., from 620 kyr to 64 kyr). This is an interesting result that is explained by the fact that K is the only true rate parameter in the equations we have used to describe the behaviour of the

570 sedimentary system. As shown by Yuan et al. (2019), the response time scale of a system governed by equation 2 behaves as:

$$\tau_G \propto (1+G)^{1/n} U^{1/n-1} K^{-1/n} L^{1-pm/n} \tag{19}$$

where L is system length and p is Hack's law exponent (≈ 2). For $n = 1$ and $m \approx 0.5$, as assumed here, we can write:

$$\tau_G \propto (1+G) K^{-1/n} \tag{20}$$

Assuming that $\upsilon \propto \tau_G$, this explain the dominant dependence of υ on $1/K$.

575 Changing, F, β, and G (see Figure 14) has a minor impact on the autogenic recovery time υ. For example, increasing β by an order of magnitude to cause the topography to change from concave to convex shape ($\beta = \alpha/10$ vs $\beta = \alpha$), increasing F from filling (eg: $F = 2.5$) to high bypass conditions (eg:$F > 10$), or moving from highly transport limited ($G = 1$) to supply limited ($G = 0.2$) conditions all tend to slightly decrease υ), i.e., within approximately a 100 kyr range (Figure 14).

5   Discussion

580 ## 5.1   Subsidence vs. Autogenic Grain Size Fining

We have seen that under certain circumstances, namely high F-values, low β-values or high G-values, the grain size fining predicted by GravelScapeMCH deviates markedly from Duller et al. (2010)'s predictions. Recall that, F is the ratio of flux
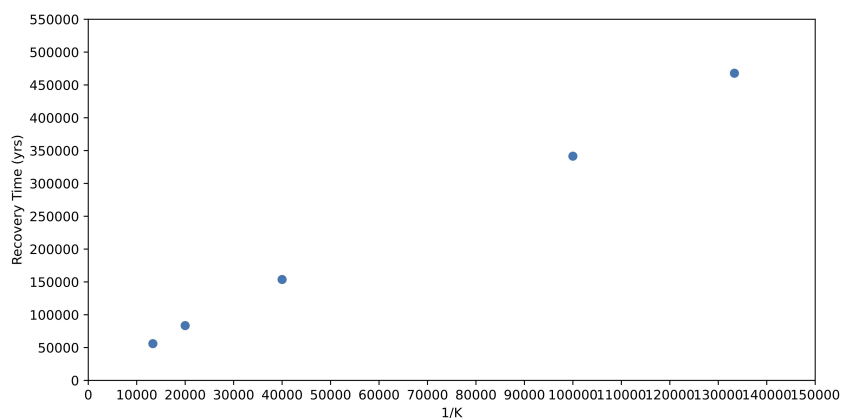
Figure 15. The correlation between $1/K$ and recovery time with all other variables in the model set up held constant.

relative to integrated subsidence (controlling sedimentation and bypass), β is the ratio of upstream vs downstream discharge dominance (controlling fan extent and topography), and G is the transport coefficient (controlling the transport vs detachment

585   limited nature of the system). We have shown (see Figure 13) that these deviations are proportional to the contribution to sedimentation from autogenic processes, which we quantified by introducing a depositional divergence factor. We therefore propose to differentiate between two main regimes for grain size fining: 1) the subsidence-dominated regimen (grain size divergence < 0.05) where subsidence is the dominant control on grain size fining and 2.1) the autogenic dominated regime (grain size divergence > 0.05) where purely autogenic dynamics controls fining and 2.2) a mixture of subsidence- and autogenic-dominated

590   (or mixed) regime where both impact the total grain size fining rate. In Figure 16A and B, we now map the boundary between these regimes (based on grain size divergence) in the $[F, \beta/\alpha, G]$ parameter space. We have also indicated another grain size fining regime of local minima dominated fining corresponding to situations where 30% or more of the basin becomes dominated by local minima. However, the local minima regime varies heavily depending on G and K in addition to F and β so the exact position of this transition is somewhat arbitrary. In Figure 16C and D, we also show the total main channel fining (i.e.,

595   main channel outlet dimensionless grain size) in the same region of the $F - \beta$ parameter space than in the corresponding A and B panels.

     In the $G = 1$ case (Figure 16A), the subsidence-dominated fining regime (grain size divergence < 0.05) occurs for simulations with a $F < 4$ or $\beta => \alpha$. In the $G = 0.2$ case (Figure 16B), the entire parameter space is in the subsidence-dominated or local minima dominated regimes. To the contrary, in the $G = 1$ case, fining is dominated by autogenic or mixed processes for

600   values of $F > 4$ and $\beta < \alpha$, i.e., systems that are in by-pass or small compared to the basin flexural wavelength.

     Note that if estimates of F, β or G are not available, we can still determine if we are in a subsidence dominate regime based on the total grain size fining. Indeed, comparing Figure 16A and C (and in agreement with the results earlier in figure 12 and 14), we can also deduce that, regardless of β, or F, a total grain size fining $>= 0.3$ (or grain size $<= 0.7$ at the outlet) within
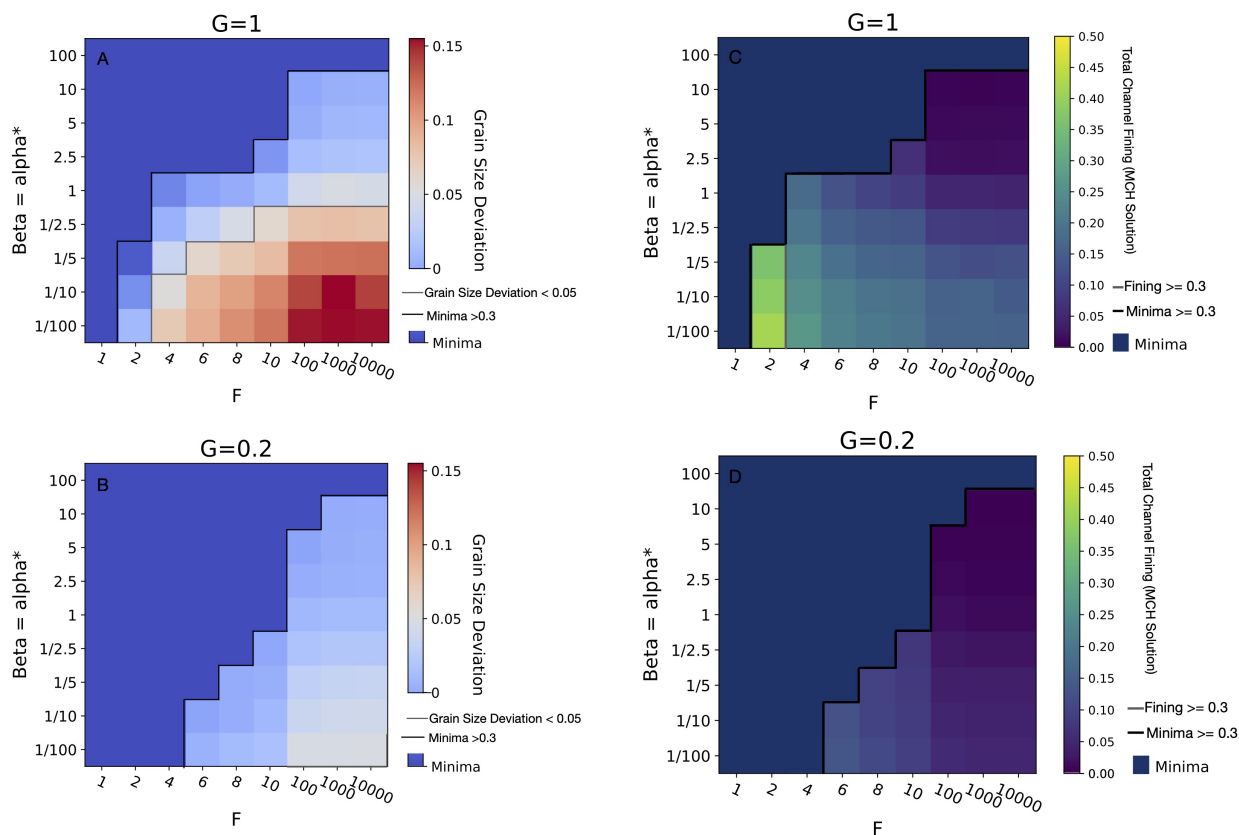
Figure 16. The left side plots show contours of grain size divergence as a function of F and β for A) $G=1$ and B) $G=0.2$. Dark blue regions correspond to model runs where more than 30% of the model was influenced by local minima. The local minima boundary is somewhat arbitrary as it can be reduced with increasing G and decreasing K in addition to the β and F under analysis. The right side plots show contours of total main channel fining as a function of F and β for C) $G=1$ and D) $G=0.2$. Positive grain size deviation entails greater fining in the GravelScape$M$CH solution relative to the GravelScape1CH. Grain size fining or deviation from different model set ups of F, G, and β, were average over steady-state, across the basin, and downstream to produce one value for each model set-up that fills a raster cell.

the stratigraphic record is most likely indicative of a long-term (steady-state) subsidence dominated fining because, for these
605   high fining rate examples, autogenic grain size fining is limited or short lived. In other words, when fining greater than 0.3 is observed, and GS deviation is under 0.05, it appears relatively reliable to use grain size fining to derive estimates of subsidence as has been done by many researchers (Duller et al., 2010; Whittaker et al., 2011; D'Arcy et al., 2017). Note, however, that increasing G above our numerically-limited value of 1 could theoretically increase the extent of the autogenic-dominated fining domain in the $F-\beta$ space. There is also evidence that real-world basins are often transport limited and thus characterized by
610   a high G value (Guerit et al., 2019), which would favour the prevalence of autogenically influenced grain size fining.

The situation is more complicated if one observes small, i.e., < 0.05, or no fining, that is if the grain size at the outlet is > 0.95. Several cases must be considered: the system is 1) under high by-pass with a large fan and ample sediment (high F, high β, and G=1) (figure 16C), 2) under high bypass regardless of its β in the case where $G = 0.2$ (figure 16D), 3) strongly affected by local minima (figure 16C and D), or 4) experiencing a transient pulse. Thus, it is tempting to assume that with a

615 total fining of less than 0.05 the system is in high bypass. However, subsiding basins (low F) often record large coarse grain pulses (Quick et al., 2023; Armitage et al., 2011) of short duration with little fining that seem to correspond to high precipitation events, that may cause a large increase in β if the excess precipitation is limited to the source area.

There exists also a mixed regime where autogenic processes are not negligible and subsidence is large and can equally control fining, typically when $F => 4$ and $F < 10$ for $G = 1$. In these experiments, grain size divergence is low but not negligible,

620 i.e., between 0.05-0.1 (16A) and total fining rate is in the range 0.1 to 0.3 (16C) implying a non-negligible contribution from subsidence. The position of this transition between the purely autogenic regime and the mixed regime will vary depending on G (figure 16) and is therefore somewhat arbitrary. The key point to remember is that, within total fining ranges of 0.05-0.3, autogenic processes are likely to impact grain size fining and interpreting it to derive subsidence patterns should be done with caution. Grain size interpretation in this range runs the risk of over-interpreting subsidence rate or under-estimating F (i.e.,

625 the by-pass rate) due to autogenic processes impacting grain size fining. For example, interpreting subsidence from grain size fining within the autogenic regime could lead to an estimate of $F = 5$ (based on an observed total fining of 0.85 at the outlet in Figure 12 using a 1CH approach) and a non-negligible subsidence, when, in fact, the real value of F is likely to be greater than 100 without any substantial subsidence because the fining is controlled by autogenic processes in a low β configuration.

5.2 What can we learn from fining in high by-pass system?

630 Concerning F, high bypass is not synonymous with high flux (although this may often be the case), as systems with very low flux entering and leaving the basin with no subsidence would still produce a high F and be highly autogenically influenced (although not much of this system would be preserved). This highlights the extreme importance of accommodation space in determining the possibility of the autogenically influenced regime. Due to this, any pre-existing topography that would add to accommodation space or raise the basin prior to the onset of a given external forcing event under analysis is relevant to

635 determine the time it takes for the system to move into a filled and autogenic state and the autogenic nature of the system in question.

At steady-state, if we know that the system is in by-pass (no or little subsidence) and yet observe substantial fining, we can safely assume that the fining is controlled by autogenic processes. Under high bypass, the fining becomes a function of β, which, in turn, can be related to the size of the source catchment (or the sedimentary fan) relative to the subsidence pattern

640 (or flexure wavelength): the smaller β, the stronger the fining. Noting that most sedimentary fans are smaller than the flexural wavelength of the lithosphere (Braun et al., 2023), low β-systems should be the most common. Most notable exceptions are mega-fan systems.

In a high by-pass system, variations in grain size fining are difficult to interpret due to the condensation of the stratigraphic record. They can arise from either variations in β related to variations in precipitation rate between the source area and the

645   basin or, changes in downstream basin area that alter discharge, flux, and subsequent autogenic dynamics. Although, this work
       has focused on the impact of changing β through precipitation gradients. Changing base-level (I.E: basin area) and drainage
       divide capture (I.e. catchment area) would impact β and subsequent autogenically induced grain size fining rates. Caution
       must therefore be used in interpreting variations in grain size fining as evidence for variations in rainfall patterns without first
       constraining that the catchment and basin configuration.

650   High by-pass systems can be characterised by high rugosity, which should therefore be more easily quantifiable from the
       stratigraphic record or the relief of present-day topography in active sedimentary systems. In high by-pass systems, depositional
       divergence rate can also be equated with local depositional rate (as subsidence rate is small). This implies that first-order
       estimates of the autogenic recovery time (defined as the ratio of rugosity by depositional divergence rate) can be obtained
       from the stratigraphic record, and, in turn used to provide estimates of the erosional constant K, a parameter that is difficult to
655   estimate especially in depositional environments.

5.3   Natural examples

Natural systems cover a wide range of the $F - \beta$ parameter space. Extension in the Basin and Range area (Norton, 2011) has
lead to high subsidence and accommodation rate in the Death Valley graben (Hammond et al., 2012) resulting in an under-
filled to early fill sedimentary basin with an active depositional surface that presently lies 86m below sea-level (Burchfiel and
660   Stewart, 1966) and where large lakes frequently form (Blackwelder, 1933; Grasso, 1996). This indicates low F conditions
       and an ideal situation for subsidence dominated grain size fining (eg: (D'Arcy et al., 2017)). Megafans exiting the Himalayas
       (eg:Kosi) have a convex or linear topography (Chakraborty et al., 2010) indicating a large β value (shown in Fig. 3) that is
       likely to minimise autogenic deviation (top portion of figure 16A).

In other areas such as the western Coastal Cordillera of northern Chile (Walk et al., 2020) or along the Skeleton Coast of
665   Namibia (Walsh et al., 2022), sedimentary fans forms with little or no subsidence of the underlying basement and must therefore
       be characterised by high F-values. These high by-pass systems are in the autogenic fining regimes and their stratigraphy is
       likely to record variations in β or fan extent related to variations in precipitation/climate (right portion of figure 16A). This
       would explain the apparent climatic/precipitation control on fan morphology evidenced by Walk et al. (2020) . However, some
       of these fans have their size limited by their vicinity to the coast, preventing them from responding to variations in precipitation
670   rate in their upstream area (Walk et al., 2019).

High F or by-pass systems can also be found near 'mature' orogenic settings such as the Alberta Basin of southern Canada
       where subsidence and in-filling rate has greatly decreased since the onset of collision in the Jurassic and again in the Cretaceous
       (Mossop and Shetsen, 1994). The sedimentary fans that form adjacent to the Canadian Cordillera have much smaller extent
       than the flexural wavelength of the underlying old cratonic lithosphere (Koohzare et al., 2008), implying a small $beta$ value.
675   These systems are located in the bottom, right portion of the F-β plane shown in figure 16A) and are thus likely to be in the
       autogenic-dominated fining regime as suggested by an overwhelming presence of internal processes within post-glacial fans in
       southern Alberta Campbell (1998).

5.4 Identifying Subsidence vs Autogenic Dominate Regimes in the Stratigraphy and Geomorphology

GravelScape can be used to simulate a three-dimensional stratigraphic record in a subsiding sedimentary basin. In order to
680   identify an autogenic vs subsidence dominated regime, our simulated stratigraphy and grain size fining can be used for comparison with natural systems to derive information about the depositional environment and conditions. To illustrate this point, we show in Figure 17, various sections through a series of three model experiments that show the stratigraphic architecture as well as the patterns of grain size fining in plan form predicted by GravelScape. The top panel (A) corresponds to a model with high F values and low β/α values (high bypass and thus autogenic dominated fining with concave topography), panel
685   (B) corresponds to a model with high F and $\beta=\alpha$ (high bypass and thus autogenic dominated fining with convex topography) and panel (C) corresponds to a model with low F and low β (low bypass and thus subsidence dominated grain size fining with concave topography). None of these models are strongly affected by local minima (under 0.3 percent of the basin). In each panel, we show contours of predicted grain size values along a vertical cross section from mountain to base level in the center of the model (sub-panel 1), along the entire surface of the model at the last time step (sub-panel 2), and along two vertical
690   cross-sections (sub-panels 3 and 4) perpendicular to the first one at two locations along the x-axis as indicated by red lines in the first cross section and the top surface view. Note that the vertical cross-sections (in both x- and y-directions) cover time steps (and thus depth) from the second half of the model evolution only where steady-state conditions have been reached. We have plotted grain size values only in 'major channels', i.e., defined as where discharge is greater than a threshold discharge (see methods for description) and filled the remaining areas or 'floodplains' in dark blue. This was done to emphasise major
695   channels, channel mobility, and channel reworking. Within the stratigraphic transects, channel mobility can be estimated from the shape of the channels and the proportion of the basin they covered. Rugosity can be estimated by considering topographic relief shown and by the amplitude of the cross-cutting patterns of infilling and incision within the across basin stratigraphy in sub-panels 3 and 4. Alternatively, evolution of channel mobility and rugosity with changing F during basin evolution can also be seen in Fig. A4.

700   When subsidence dominates the stratigraphy (Figure 17C), it controls the rapid (> 0.3) grain size fining rates within the channel (Figure 17C1 and C2), preservation is high (thick stratigraphic layers in Figure 17C1), the across basin rugosity is low (no reworking, little topographic variation, or incising/cross-cutting of channels in Figure 17C3 and C4), and the channel mobility is high, distributing channel grains evenly across the basin (Fig. 17C3). Relative to the high bypass example (Figure 17A1 vs C1), the topography in the fan is depressed/lower due to the high subsidence rate. These results agree with observations from
705   the Ganges Plain by Dingle et al. (2016), for example, that show rapid downstream fining in perched channels that are prone to mobility and flooding of their banks within the rapidly subsiding portion of the basin. Alternatively, slowly subsiding portions of the same basin display higher surface topographic slopes, greater incision by channels (less mobility), and the further propagation of a coarse grain front within the channel (Dingle et al., 2016). With abundant sediment supply, Mackey and Bridge (1995) show that channel belts shift more and towards areas of maximum subsidence unless sufficient depositional (inherited)
710   topography remains. Then, diverted channels follow the maximum floodplain slope locus (Mackey and Bridge, 1995). This positive relationship between avulsion and sedimentation rates under high subsidence, is reflected in our model stratigraphy in
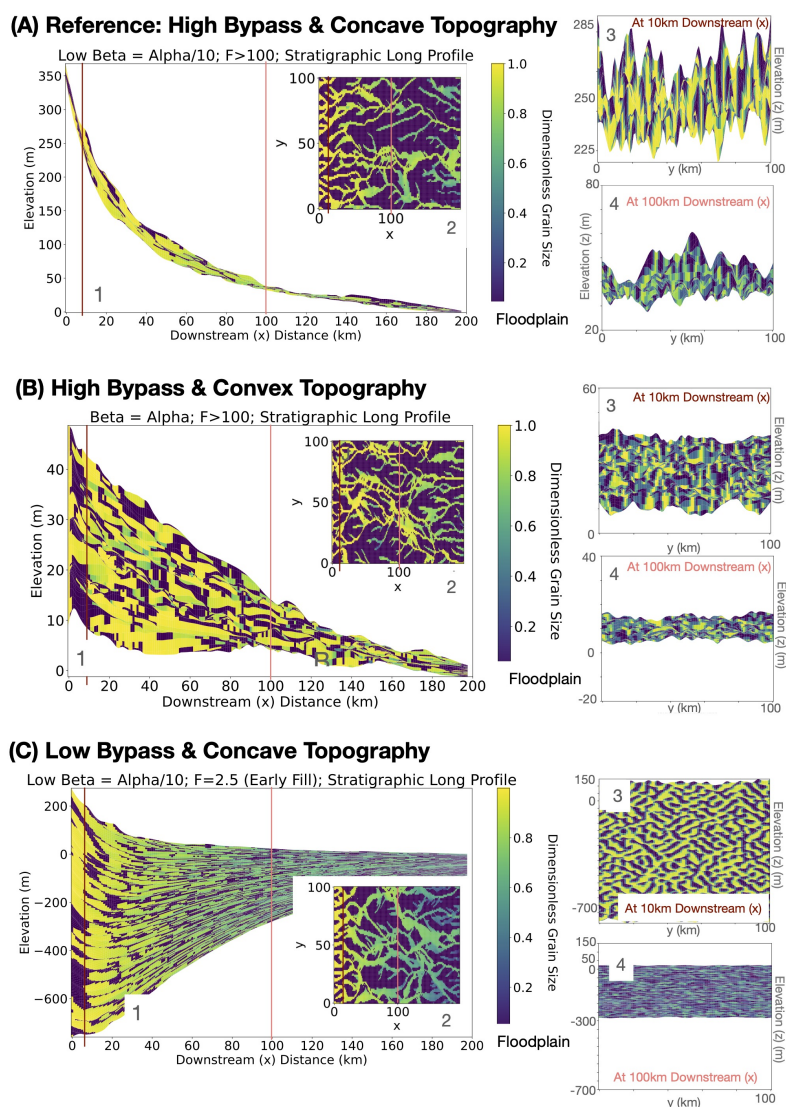
Figure 17. Different stratigraphic cuts (1-4) through the basin to show channel grain size fining, channel movement, stratigraphic thickness, rugosity/ channel cross-cutting and reworking under (A) high bypass with a concave topography, (B) high bypass with a convex topography, and (C) low bypass with a concave topography. Wherever coarse gravel grains were not deposited during a given time step was filled in dark blue as floodplain. Plots 1 show a long profile stratigraphic cut through the basin. Plot 2 shows a plan view of the model surface at the final time step. Plots 3 show the across basin stratigraphic cut at 10km downstream within the basin showing the floodplain (dark blue) and coarse grain size within the channels. Plots 4 show a across basin cut further downstream in the basin. All stratigraphic plots were made with a G=1 and K= 2e-5 and the only input variables that changed between plots where either upstream precipitation (changing β) or the imposed underlying subsidence (changing F).

the proportion of coarse grain channels distributing sediment across the basin without any reworking as shown in figure 17C3 and by the correlation shown in figure 14 between channel mobility and deposition rate.

When vertical accommodation is minor (Figure(17A and B), stratigraphic results show generally less (< 0.3) grain size
715 fining within the channel and much less stratigraphic thickness relative to Figure17C since there is less overall accommodation/sedimentation. Sedimentation that does occur is controlled by local lateral and longitudinal (x and y) accommodation space within the topographric profile that responds over time to pulses of incision and deposition leading to strong depositional divergence. Rugosity, and cross-cutting/reworking of channels within stratigraphic packages is high (Figure 17A3). Comparing Figures 17A and B, we note that topography, rugosity and cross-cutting are greater with lower β. Channel mobility is
720 lower under bypass rather than filling conditions (Figure 17B3), but comparing the two bypass solutions (Figure 17A3 vs B3 proportion of coarse grains), we see that channel mobility is slightly higher under scenarios with higher topography/steeper slope or lower β-values. The channel mobility results agree with descriptions of (Mackey and Bridge, 1995), of a topographic control (higher topography shows higher mobility) when subsidence induced sedimentation is null. Also in agreement with our autogenic-dominated stratigraphic results, Straub and Esposito (2013) state that rapid migration (channel mobility) and deep
725 channels (producing a high rugosity) when paired together relative to a low system aggradation (high bypass) produced the highest system reworking.

Throughout the paper we have described how, within the autogenic regime, lower β induces higher autogenic dynamics and fining. This is because of the higher incisional/depositional energy induced from higher topographic slopes under low $beta$ conditions. This lateral and downstream variability controls accretion, infilling, and incision, and, ultimately, grain size
730 fining. Farrell (2001) describes in the Saskatchewan river and its stratigraphic record, phenomena similar to the model. For example, they note that the system would laterally accrete into topographic lows to fill them. If favorable accommodation space developed downstream, the flow would channelize to reach and infill (dropping its load and therefore fining in) these areas along the profile (Farrell, 2001). Comparable to our higher cross-cutting, reworking and rugosity in the low β case (17A), Skelly et al. (2003) have observed that channel belts become more dissected and incised by smaller channels as discharge
735 decreases. Alternatively, under high discharge, secondary channels, islands, and bars become flooded to form larger channels (Skelly et al., 2003) and flatter topography. Thus, under bypass, the system becomes more sensitive to variations in lateral and down-basin topography induced through drainage and incision/deposition variations in accommodation space that is greater under higher slopes (low β).

5.5 Flexural Foreland Basins: Evolving from Subsidence to Autogenic Dominant Conditions

740 So far, we have performed numerical experiments assuming an imposed, constant subsidence function to mimic Duller et al. (2010)'s 1CH setup and compare our MCH predictions to theirs. This idealized situation is characterized by a parameter F that represents the degree of by-pass experienced by the basin. In natural settings, it is well documented that this by-pass level evolves through the orogenic or collisional cycle, and to understand this evolution one needs to consider the effect of flexural isostasy, which is the key process controlling subsidence in the foreland basin under the weight of the mountain topography
745 (Beaumont, 1981). To mimic foreland basin evolution, we coupled FastScape to a flexural model (Figure 18) that assumes that

the Earth's continental lithosphere reacts to vertical loading and unloading as a thin elastic plate (Turcotte and Schubert, 2002). This model does not include horizontal advection. Within the foreland basin presented (Figure 18) , we chose a $\beta <= \alpha$ set up to allow for potential autogenic dynamics under a concave topography that avoids potential high local minima scenarios (Fig. 16) and have divided foreland basin evolution into four phases based primarily on F and deposition/erosion rates. Additional

750 evolution of autogenic components (channel mobility (decreasing with increasing F) and rugosity (increasing with increasing F) under the same $\beta <= \alpha$ set up are shown in the Fig. A4. Basin evolution with $\beta > \alpha$ shows less autogenic grain size fining, more rapid evolution into the bypass state, long periods of erosional unconformaties, and greater back-infilling in the outer (downstream) margins during the later stages basin evolution (Fig. A5). Early in the collision, during what we shall call
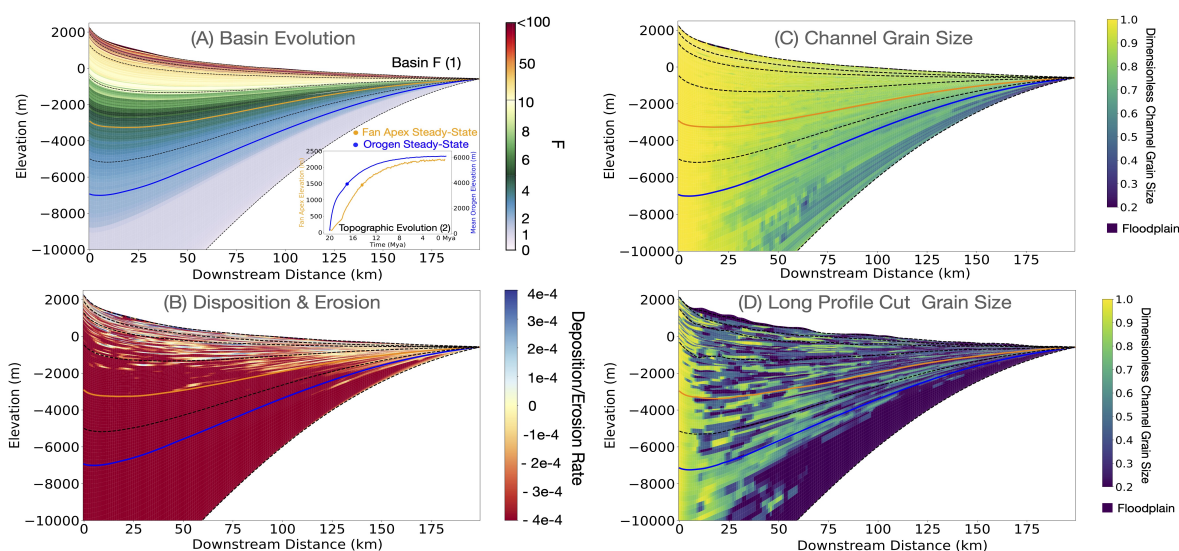
Figure 18. Foreland basin evolution with the addition of flexure rather than imposing underlying subsidence conditions. We describe the flexural evolution of a foreland basin before and after the orogen (blue line) and fan apex (orange line) reach a steady-state topographic elevation. The exact position we define as having reached steady-state (the point within 63 percent (SPL standard) in height of the maximum topography) is shown in the A2 inset plot as a blue (orogen) or orange (fan apex) point. Basin evolution of F (A1), deposition and erosion (B), channel grain size (C), and a long profile cut through the basin (at across basin distance Y=10) exposing non-channel (or blue floodplain) and dominant channel (yellow-green) locations with associating fining (D) foreland are shown. The simulation ran for 20Myrs (1000yr time step), with a K=7.5e-5, G=1, 50 km orogen, 200 km basin (1000 m cell length), Uplift of 0.01 $myr^{-}1$, elastic thickness of 20e3, asthenosphere density of 3200, lithosphere density of 2800, basin precipitation of 1, and orogen precipitation of 0.8 producing a lower $\beta <= \alpha$.

Phase 0 (whitish blue $F<1$ in Figure 18 A1), mountain topography and thus basin subsidence rapidly grow but relatively
755 little sediment is produced yet; this leads to a mostly 'starved' foreland basin. The corresponding by-pass ratio, F, is therefore very low inducing rapid channel fining (Figure 18 C) and the basin infilling is most likely lacustrine or marine without a far

progradation of coarse channels (see base of Figure 18 D). Since our grain size solution is not suited for these depositional environments, we will not deeply discuss Phase 0.

During Phase 1, 5<F>1 (shown in blues in Figure 18 A1) indicating a subsidence dominated regime (see Figure16 for
760 $\beta = \alpha*1/5$) where subsidence induced fining is greater than that of autogenic dynamics) with thick stratigraphic packages (approx. -15km to -7km) deposited in less than 4Myr (dotted line). The deposition rate is consistently higher at the mountain toe and lower in the outer reaches of the basin (Figure 18 B) and progressively decreases over time. Topographic slope, erosion rate, and subsequent flux has increased in the mountain steadily to ultimately balance the subsidence rate caused by the evolving topography; the by-pass ratio, F, has reached 1 and continues increasing as the basin fills. During phase 1, subsidence domi-
765 nated fluvial grain size fining rates decrease as F increases (Figure 18 C and D). This produces coarsening upwards within the strata. Channel mobility events are very frequent (almost one every time step) causing very few floodplain areas (Figure 18 D and Fig. A4) and rugosity is low (Fig. A4) and not well preserved as vertical accommodation dominates.

Phase 2 (shown in green in Figure 18 A1) is a transitional phase when the basin first enters a mixed autogenic regime 5<F<10 (subsidence induced fining is still quite high, but autogenic dynamics may already be altering the fining rate to some
770 degree as shown in Figure 16) and in this case, as the basin (orange) approaches steady-state. During phase 2, we begin to see greater variation in deposition rate and may even see erosional unconformities in the outer reaches of the basin (Figure 18 B. This erosional phase often initiates in portions of the basin where the subsidence curve is nearly flat or convex.

Between phases 1-2, as the mountain tends towards topographic steady-state, the mountain load stops increasing, flexure-driven subsidence decreases and ultimately (at least the portion due to tectonic loading) stops while sediment flux reaches a
775 steady-state value that corresponds to the tectonic flux (convergence rate) into the orogenic area. Subsidence generated after orogenic steady-state (phase 2) is due to the sediment loading. After this decrease in subsidence due to reaching orogenic steady-state, and with a constant flux from the orogen, the basin is infilling to eventually reach a steady-state fan apex height (orange) some time after the orogenic (blue) steady-state has been reached. In this mature phase of evolution (after orogenic and especially after basin steady-state), the system transitions into a progressive by-pass regime in which the value of F increases
780 to very large values. Keep in mind that this is in a model in which there is no horizontal advection. In a natural system, the lower plate would continue to be horizontally advected such that the overal shape of the basin would be in steady state, but the subsidence of any vertical section would keep increasing as they move towards the mountain main thrust.

By Phase 3, the basin has been sufficiently infilled with little vertical accommodation space producing topography well above base level and F>10 (Figure 18A). This phase undergoes purely autogenic dominated fining where any fining occur-
785 ring is likely autogenic and under 0.2 (relatively coarse) (Figure 18C and 16). Phase three shows the highest variation in the deposition and erosion rate in the upper reaches of the basin (Figure 18 B). Stratigraphic packages are thin and erosional unconformities can develop that can extend across the entire basin and grain size fining varies depending on the depositional/autogenic processes. Channel mobility is lower than during the purely subsidence dominated regime (phase 1) producing more floodplain areas dispersed between the channels (Figure 18 D, but reworking may cause some channel amalgamation never
790 the less (especially if β was lower). Shown in A5, under more erodible settings (higher precipitation) with ample discharge, the basin can undergo multiple Myr phases of erosional bypass followed by infilling at the base or middle of the profile and

propagating upwards. During high bypass, infilling will occur where, along the profile, the most accommodation is generated, for example, through sediment loading or erosion.

Unlike in our model simulation, foreland basin evolution is not always linear as there can be pulses or uplift and subsidence raising and lowering F within the basin and potentially pushing in and outside of the bounds of subsidence or autogenic dominated fining. This of course also depends on the magnitude of autogenic dynamics relative to subsidence that we have altered in our approaches through β. Thus, the autogenic dominated regime is relevant, not just in the final stages of basin evolution, but can also matter whenever during the basin evolution, the subsidence is substantially reduced relative to the autogenic dynamics. Although, the model presented above was not meant to reproduce the exact evolution of a real-world basin, we will use it as a comparison to study an example of a foreland basin that transitions from under-filled to over-filled conditions, i.e., the Western Canada, and more specifically the Alberta foreland Basin (Catuneanu, 2004; Mossop and Shetsen, 1994; Leckie and Smith, 1992; Beaumont, 1981) for which we show a stratigraphic cross-section and paleogeographic maps for selected geological times in Figure 19. Although there is clear evidence of a N-S diachronous evolution of the collision and basin development (Mossop and Shetsen, 1994; Poulton et al., 1990), we will focus our comparison of model predictions to the general evolution of the system in mid-southern Alberta (between Swan Hills and Cypress Hills area) from mid-Jurassic onwards generally avoiding issues related with basement structures, namely the underlying (Peace and Sweetgrass) arches (figure 19).

The basin formed by flexure associated with the accretion of the Intermontane Superterrane against western Canada in the Jurassic to form the early Rocky Mountains/Columbian Orogen ((Earle, 2015; Mossop and Shetsen, 1994)). Within the upper Jurassic (Figure 19 A (dark green) or B6), central-southern Alberta exhibited subsidence in response to early mountain building and was inundated by a shallow seaway accumulating thick marine shales. This could represent phase 0 in our model where the basin is underfilled, its surface is below base-level, any coarse fluvial sediments are not propagated far, and the grain size fining regime is largely non-fluvial or subsidence-dominated.

After an initial phase of mountain building there is a well defined erosional unconformity which corresponds to a tectonic quiescence and rebound episode in the Canadian Cordillera from 140 to 125 Ma (Leckie and Cheel, 1997) whereby previous work suggests long-wavelength uplift may have occurred due to unloading of the orogenic front (Johnson and Dalrymple, 2019). Following this unconformity is an extensive alluvial facies called the Cadomin Fm made of clast supported, subrounded, dominantly coarse conglomerates (with local sandstone occurrences) and hundreds of kilometers in spatial extent in a fluvial system flowing northly (Johnson and Dalrymple, 2019; Leckie and Cheel, 1997) to easterly (McLean, 1977) for 12-18 millions of years during roughly the Barremeian-Aptian (White and Leckie, 1999) (Figure 19A (above the dark green) or B). As evidenced by the erosional unconformity and propagation of coarse fluvial grains, the basin has rapidly entered a state of high bypass and potentially a highly autogenic dominated (eg: $F>10$) regime due to rebound. The Cadomin Formation has a relatively uniform thickness across the entire basin, suggested that it marks the end of the flexural subsidence driven by the load of the mountain/orogen growing and a transition to subsidence driven by the load of the sedimentary basin itself. This explains its relatively well preserved thickness in a general bypass context.
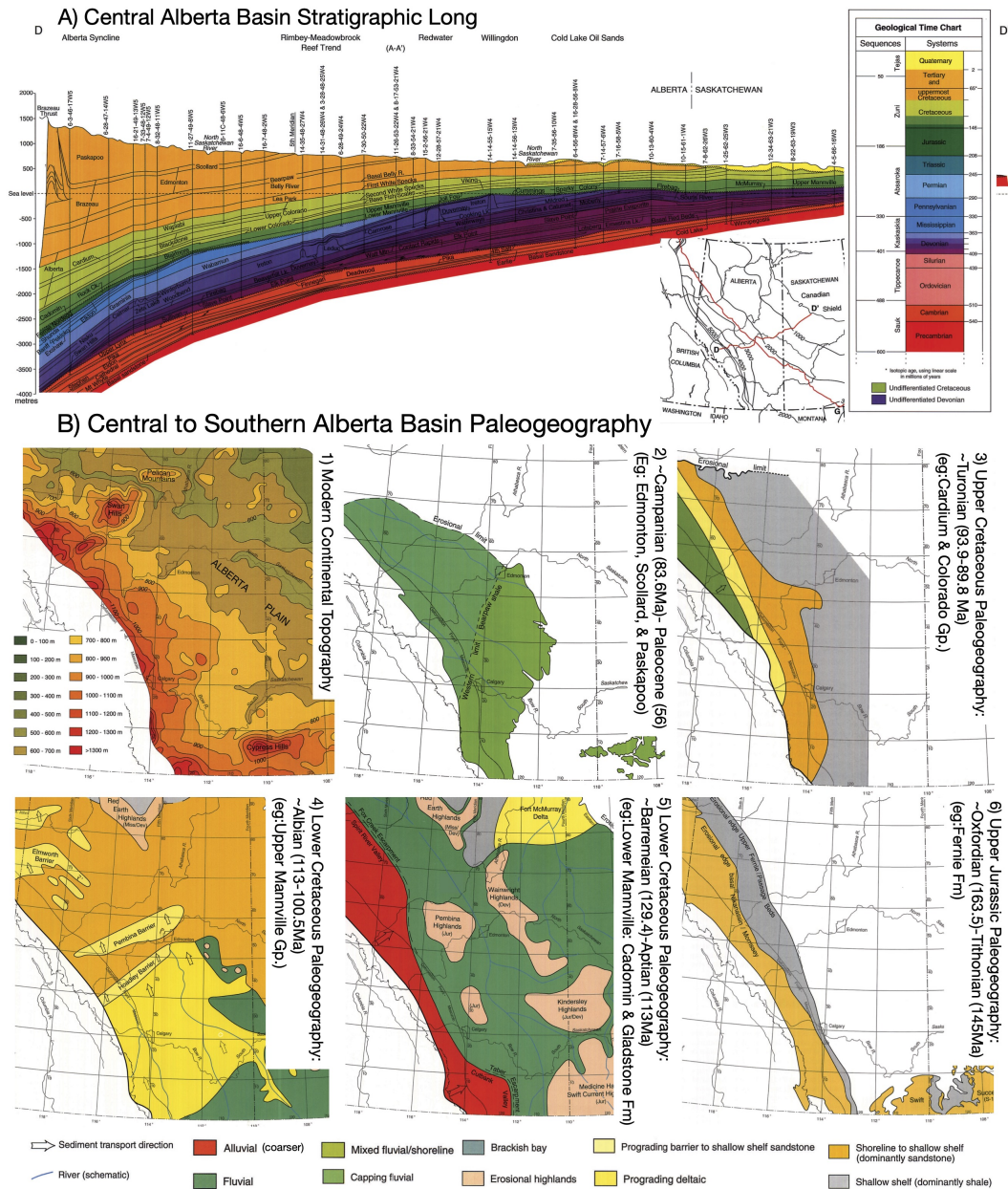
Figure 19. images were compiled and modified from the Atlas of the Western Canada Sedimentary Foreland Basin (Mossop and Shetsen, 1994) under the Open Alberta Licence (*https://open.alberta.ca/licence*). Panel A shows shows the stratigraphic thicknesses and ages perpendicular (D to D') to the orogen and 'downstream' (x) within the central Alberta foreland system south of Edmonton. The exact stratigraphic D-D' transect location is shown on an inset map of western Canada in subset A. Subsets B show the modern topographic elevation (1) or paleogeography (2-6) with fluvial propagation vs marine inundation extents at several time intervals between the upper Jurassic (Figure B6) to present(Figure B1).

There is evidence within the Cadomin Fm of an autogenic regime potentially within a high bypass (described above) and a generally low beta (further promoting autogenic dynamics) setting. However, there could have also been some climate seasonality (Johnson and Dalrymple, 2019; Jablonski and Dalrymple, 2016) around this time to impact the grain size signal and β (eg: seasonality indicated from banded argillans observed within the soil by (Johnson and Dalrymple, 2019)). The generally

830   low beta is inferred from 1) a large basin area where the upper Cadomin Fm is several hundreds of kilometers long from the northern shoreline (Smith and Leckie, 1990); and 2) sources indicating a generally semi-arid climate (eg: silcrete in these paleosols) for western Canada around the Jurassic-early Cretaceous transition (Leckie and Cheel, 1997; Leckie and Nadon, 1997; Ludvigson et al., 2015) making an average high precipitation in the catchment forcing an, on average, high beta unlikely. The Cadomin is described in areas as a megafan similar to the Kosi, but coarser and with some preserved evidence of auto-

835   genic dynamics (Leckie and Cheel, 1997). Amalgamation, frequent shifting, and bank cutting of channels described within the stratigaphy (Leckie and Cheel, 1997) match our stratigraphic results of an autogenic dominate fining system under very high bypass with reworking (figure 17). Recent work has identified terraces in the upper basin preserved in the stratigraphy (Johnson and Dalrymple, 2019) that are indicative of aggrading and incision pulses (similar to our depositional divergence) during this period, that have been interpreted in relation to climate cyclicity (a possible β signal) and erosional knickpoint propagation.

840   Well sorted and poorly sorted episodes within the conglomerate are described as potential inter-flood episodes with reworking (potentially a lower β with more autogenic dynamics) and flood episodes (a potential raise in β with a lower autogenic signal) without time for sorting (Johnson and Dalrymple, 2019). Johnson and Dalrymple (2019) also makes the point that climate seasonality during the Cretaceous would have been less than what we have observed in the later Quaternary. This makes it likely that any fining or changes in fining within the Cadomin Fm are likely due to internal dynamics or an autogenic response

845   to the climate seasonality propagating through the basin.

Following tectonic quiescence, mountain building reactivated in the Cretaceous when the Insular Superterrane collided with North America and increased the eastward thrusting of the Intermontane Superterrane. Subsidence resumed as well. Throughout the Albian, there are varying extents of brackish bay, delta, and shallow marine shelf deposits whereby any fluvial propagation of coarse grains that was observed in the Cadomin Fm is significantly reduced (eg: Figure 19 A (light green) or

850   B4). The foreland trough, parallel to the Rocky Mountain front, substantially broadened and deepened during the Cretaceous such that the stratigraphic preservation is much higher than in the previous upper Jurassic basin underfill interval. Based on the lack of fluvial propagation and high marine inundation, we are likely back in a phase 0-1 of basin filling. One could argue that a phase 1, early-filled basin (where F approaches and even briefly exceeds 1) occurred during select pulses throughout the Cretaceous where the fluvial and delta facies propagated further (eg: figure19B3) due to variations in uplift in time and space,

855   but any grain size fining would likely still be subsidence-dominated on account of the active mountain building. Mossop and Shetsen (1994) shows high variability in the fluvial front and marine inundation extent throughout the Cretaceous and this has also been linked to sea-level oscillations.

By the end of the Cretaceous (after the Bearpaw Fm in Figure 19 A (gold)), the marine seaway was retreating and this is described as due to the effective erosion of the mountain belt that limited its height and thus the resulting flexure, while the

860   sediment flux from the mountain continued to be high and outpaced the flexure-driven subsidence (Catuneanu, 2004). Thus, in

the Uppermost Cretaceous and into the Tertiary (Figure 19A gold (after Bearpaw Fm) and B2),the basin has entered phase 1-2 (fill) where the majority of the basin is consistently above sea-level and fluvial (dark green-mainly sandstone) sediments are transported over very long distances. However, subsidence in the western Canada retro-arc foreland basin (eg: see figure 19A), generally continued at a reduced pace during most of the Mesozoic and Cenozoic, most likely in response to the load of the
865   sediment, and allowing for the preservation of strata (Mossop and Shetsen, 1994; Leckie and Smith, 1992) and thus indicating some subsidence-mix control on grain size fining (eg: $10 < F > 1$).

Finally, the Quaternary period can be considered phase 3 in foreland basin evolution since the Alberta basin is largely in bypass or erosion (figure 19A) and the substantial Quaternary deposits with ample accommodation are in the outer basin in Saskatchewan (Mossop and Shetsen, 1994). The modern topography in the Central-southern Alberta basin on the edge of the
870   orogen is high (1000-700km in Figure 19 B1) with ample slope (promoting channel mobility and a thick active layer) and large downstream basin area (lower β) that promote high autogenic influence on grain size. Also, due to glacial rebound further promoting uplift and a high F in the south of Canada, the modern fans draining the Alberta basin are likely in an autogenic dominated regime where the impacts of β could be visible.

In summary, the Alberta foreland is one example where we would expect the basin evolving over time into an overfilled
875   and more autogenic driven grain size fining regime. This transition may not have been linear as there were periods of tectonic quiescence that could have pushed the basin into an overfilled and autogenically dominated state early in its evolution that is both well preserved and an ideal location for further applications of our model in untangling possible β signals.

6   Conclusions

We have adapted the grain size fining model of Fedele and Paola (2007) to a multi-channel system and incorporated it in a
880   Landscape Evolution Model (LEM) in which sediment transport and deposition are decoupled from the underlying basement subsidence. The model is also able to predict a range of autogenic processes such as channel avulsions and rugosity. Using the model, we have shown that grain size fining is in fact controlled by a balance between external and internal forcings, namely tectonic subsidence and autogenic processes. We have mapped the conditions under which either of the two regimes dominate: subsidence-dominated fining takes place when the basin is filling (eg: $F < 4$), whereas autogenic processes dominate in
885   controlling grain size fining when the basin is overfilled and in bypass ($F > 10$); in between is a mixed regime where the strength of autogenic dynamics relative to the subsidence (and the associated regime) depends largely on upstream relative to downstream discharge (β). Underlying subsidence (F) dominates the grain size fining rate until the depositional rate induced from subsidence becomes comparable or less than that induced from autogenic dynamics. Instead of merely shredding the subsidence signal, the grain size fining within this low subsidence, high autogenic regime, can actually provide information
890   on the climatic ratio (β) of upstream vs downstream discharge (eg: through changing precipitation gradients or upstream vs downstream area).

These predictions are in good agreement with many observations of grain size distributions in a wide variety of environments (e.g. Alberta basin), and help explain some of the discrepancies between observations and previous models that assume that

subsidence is the only driver. We highlighted how this new model can be used to help interpret grain size distributions in
895 sedimentary fans and alluvial plains. We have also shown how grain size fining evolve in a foreland basin by transitioning from
the subsidence-dominated regime into the autogenic-dominated regime. In doing so, we can already predict from the results
presented here that tectonic events are more likely to be preserved during the early phase of basin development (low by-pass,
subsidence dominated fining regime) when grain size fining is controlled by the rate of creation of accommodation space (or the
factor F) and thus convergence and uplift/subsidence rates, whereas climatic events are more likely to be recorded during the
900 late phase of basin development when grain size fining is most susceptible to variations in β. Future work should focus on how
discrete (transient) climatic or tectonic events affecting the evolution of a mountain belt would be recorded in a continuously
evolving foreland basin and, in particular, how these events would affect grain size fining patterns as done by Armitage et al.
(2011, 2013); Allen et al. (2013) assuming a subsidence-dominated fining regime throughout the life of the basin.

7 Funding Declaration

905 This project received funding from the European Union's Horizon 2020 research and innovation program under the Marie
Sklodowska-Curie grant agreement No 860383.

Code availability. Python Code for GravelScape is available. See the FastScape repository for further details:
https://FastScape.readthedocs.io/en/latest/index.html

Data availability. Data was not generated through this research.

Video supplement. We have provided several video supplements.

910 *Author contributions.*

. Amanda Wild: Conceptualization, formal analysis, investigation, methodology, software, validation, visualization, writing-original draft
preparation, writing-review and editing

. Jean Braun: Supervision, resources, software, conceptualization, methodology, validation, visualization, writing-original draft preparation,
and writing-review and editing

915 . Alexander Whittaker: Supervision, conceptualization, methodology, validation, and writing-review and editing

. Sebastien Castelltort: Supervision, conceptualization, and writing-review and editing

Competing interests. The authors declare that there are no competing interests.

Appendix A
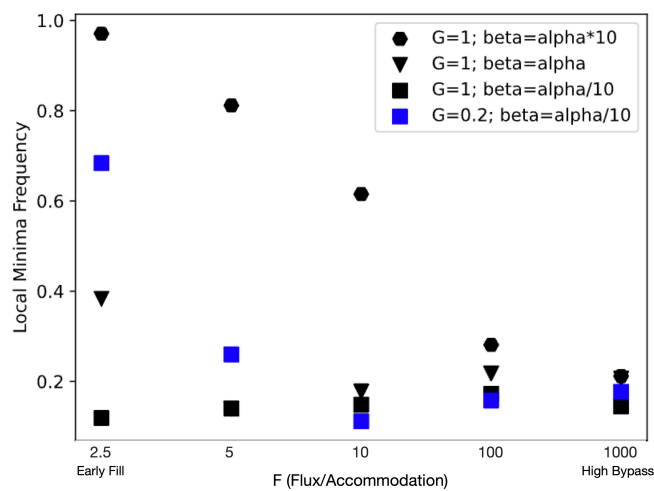
Figure A1. The prevalence of local minima covering the basin under varied stages of bypass F. The squares represent a $\beta = \alpha/10$, triangles represent a $\beta = \alpha$, and hexagons represent $\beta = \alpha * 10$. Black symbols have a G=1 and blue symbols have a G=0.2. Each square is a different model set-up of G, F, or β that has been averaged over steady-state, across, and down basin.

Acknowledgements. The authors thank Benoit Bovy for general help with xarray-simlab and FastScape curation. We would also like to thank
920 Charlotte Fillon for her comments during committee meetings and the earlier phases of this research. We would also like to thank scientists within the Earth Surface Process Modelling Section at the GFZ Potsdam and members of the S2S-Future Marie Curie ITN for their general feedback and discussions. Finally, we would like to thank Randy Enkin and members of the Pacific Geoscience Center for their general discussions and providing guided access to the Geological Atlas of the Western Canada Sedimentary Basin.
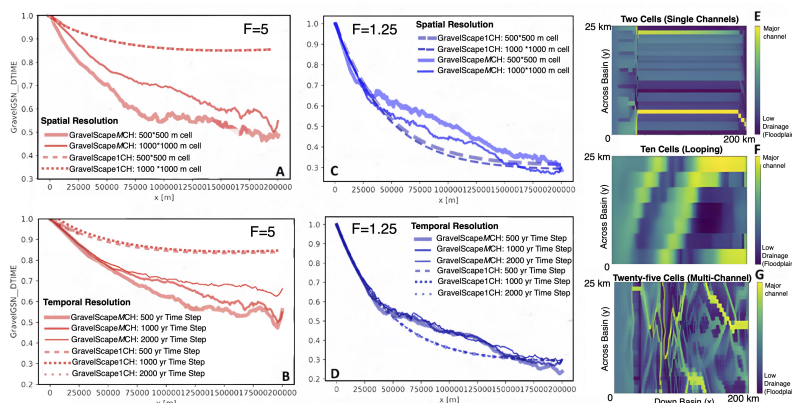
Figure A2. Shows the model grain size fining results under various spatial and temporal resolutions under a concave (low beta topography allowing for potential autogenic dynamics) with a transport-limited, high G. GravelScape1CH results are shown as dashed lines and GravelScape*M*CH results as solid lines (of various thickness and opacity depending on the spatial/temporal resolution) for F=5 (mixed-high bypass) and F=1.25 (low bypass) set ups. With the same amount of down and across basin area, panels A and C show the impact of changing the spatial grid resolution and, in doing so, changing the number of across basin and downbasin grid cells. Panels B and D shows the impact of changing the temporal resolution of time steps for the same simulation length. Shown in panel E, single channel (GravelScape1CH) 1D dynamics occur when there are only only 2 grid cells across the model and only sheet flow without multi-channel dynamics can form. Shown in panel G, after greater than circa 20 across and 40 down basin cells, the model can simulate multi-flow channel dynamics with comparable (see panels A-C for variation) GS dynamics with increasing grid cells. Lowering across (under 20) and down basin (under 40) cells shift the solution from 2D multiflow dynamics towards 1D with more interaction (eg:looping) with model boundaries (eg:panel F).

References

925

Allen, P. A., Armitage, J. J., Carter, A., Duller, R. A., Michael, N. A., Sinclair, H. D., Whitchurch, A. L., and Whittaker, A. C.: The Q s problem: Sediment volumetric balance of proximal foreland basin systems, 60, 102–130, https://doi.org/10.1111/sed.12015, 2013.

Armitage, J. J., Duller, R. A., Whittaker, A. C., and Allen, P. A.: Transformation of tectonic and climatic signals from source to sedimentary archive, Nature Geoscience, 4, 231–235, 2011.

930 Armitage, J. J., Jones, T. D., Duller, R. A., Whittaker, A. C., and Allen, P. A.: Temporal buffering of climate-driven sediment flux cycles by transient catchment response, Earth and Planetary Science Letters, 369, 200–210, 2013.

Beaumont, C.: Foreland basins, Geophysical Journal International, 65, 291–329, 1981.

Bernard, T., Sinclair, H. D., Gailleton, B., and Fox, M.: Formation of longitudinal river valleys and the fixing of drainage divides in response to exhumation of crystalline basement, Geophysical Research Letters, 48, e2020GL092 210, 2021.

935 Blackwelder, E.: Lake Manly: an extinct lake of Death Valley, Geographical Review, 23, 464–471, 1933.

Blair, T. C. and McPherson, J. G.: Alluvial fans and their natural distinction from rivers based on morphology, hydraulic processes, sedimentary processes, and facies assemblages, Journal of sedimentary research, 64, 450–489, 1994.
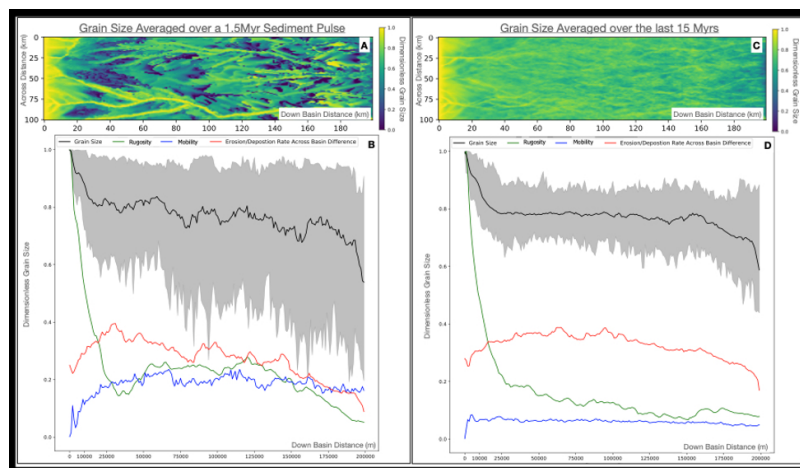
Figure A3. Although the mean trends remain the same, the method of averaging can change the results by smoothing out variation between pulses and reducing the variation across the basin. Panels A and B show the results of averaging over the approximate time a depositional wave propagates through the system (1.5 Myr in this case) in contrast to 15Myrs in panels C and D. Long profile averages shown in panels B and D display an increase in channel mobility as grain size fines leaving the fan area until reaching a maximum, relatively constant rate in the plain. The variance in deposition/erosion rate across the basin also increases after leaving the fan area and entering the early portions of the basin downstream. Rugosity (difference in topographic height across the basin) in green decreases as grain size fining, channel mobility (in blue), and deposition/erosional variance (red) increase down basin.

Bovy, B.: fastscape-lem/fastscape: Release v0.1.0beta3, https://doi.org/10.5281/zenodo.4435110, 2021.

Braun, J.: Comparing the transport-limited and ξ–q models for sediment transport, Earth Surface Dynamics, 10, 301–327, 2022.

940   Braun, J. and Willett, S. D.: A very efficient O(n), implicit and parallel method to solve the stream power equation governing fluvial incision and landscape evolution, Geomorphology, 180, 170–179, https://doi.org/10.1016/j.geomorph.2012.10.008, 2013.

Braun, J., Wild, A., Khan, S., and Malatesta, L.: Rainfall Contribution to Discharge Controls Alluvial Fan Size and Shape, international Conference on Fluvial Sedimentology 2023, 2023.

Bull, W. B.: The alluvial-fan environment, Progress in Physical geography, 1, 222–270, 1977.

945   Burchfiel, B. C. and Stewart, J.: "Pull-apart" origin of the central segment of Death Valley, California, Geological Society of America Bulletin, 77, 439–442, 1966.

Campbell, C.: Postglacial evolution of a fine-grained alluvial fan in the northern Great Plains, Canada, Palaeogeography, Palaeoclimatology, Palaeoecology, 139, 233–249, 1998.

Cant, D. J. and Stockmal, G. S.: The Alberta foreland basin: relationship between stratigraphy and Cordilleran terrane-accretion events, 950   Canadian Journal of Earth Sciences, 26, 1964–1975, 1989.

Carretier, S., Martinod, P., Reich, M., and Godderis, Y.: Modelling sediment clasts transport during landscape evolution, Earth Surface Dynamics, 4, 237–251, https://doi.org/10.5194/esurf-4-237-2016, 2016.

Carretier, S., Guerit, L., Harries, R., Regard, V., Maffre, P., and Bonnet, S.: The distribution of sediment residence times at the foot of mountains and its implications for proxies recorded in sedimentary basins, Earth and Planetary Science Letters, 546, 2020.
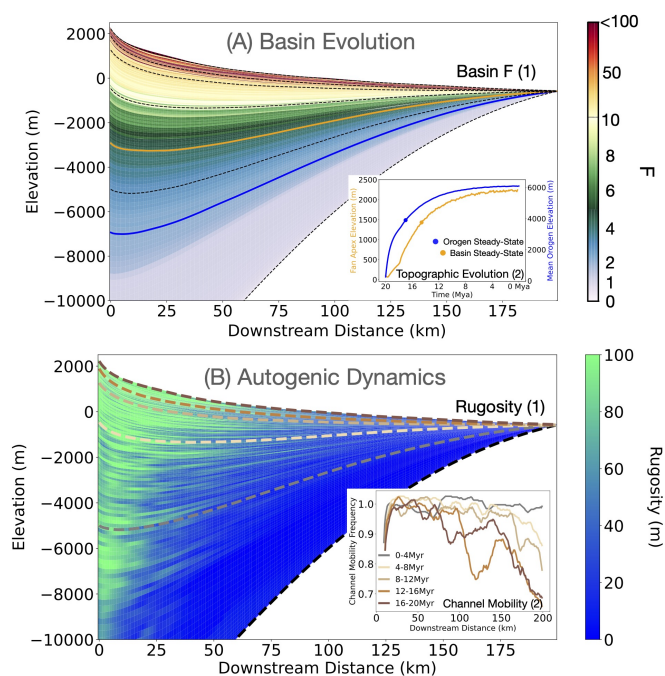
Figure A4. For a low $\beta <= \alpha$, panel A shows the basin evolution F and panel B1 depicts the corresponding rugosity (blue (low) -green (high)) and B2 the channel mobility between multiple 4Myr (brown to grey lines represent different points in time during the basin evolution) increments. Notice that as F increases the topographic rugosity increases and the channel mobility decreases. The simulation ran for 20Myrs (1000yr time step), with a K=7.5e-5, G=1, 50 km orogen, 200 km basin (1000 m cell length), Uplift of 0.01 myr^-1, elastic thickness of 20e3, asthenosphere density of 3200, lithosphere density of 2800, basin precipitation of 1, and orogen precipitation of 0.8 producing a $\beta <= \alpha$.

955   Catuneanu, O.: Retroarc foreland systems- evolution through time, Journal of African Earth Sciences, 38, 225–242, 2004.

Chakraborty, T., Kar, R., Ghosh, P., and Basu, S.: Kosi megafan: Historical records, geomorphology and the recent avulsion of the Kosi River, Quaternary International, 227, 143–160, 2010.

Clarke, L., Quine, T. A., and Nicholas, A.: An experimental investigation of autogenic behaviour during alluvial fan evolution, Geomorphology, 115, 278–285, 2010.

960   Cordonnier, G., Bovy, B., and Braun, J.: A versatile, linear complexity algorithm for flow routing in topographies with depressions, Earth Surface Dynamics, 7, 549–562, https://doi.org/10.5194/esurf-7-549-2019, 2019.

Covey, M.: The evolution of foreland basins to steady state: evidence from the western Taiwan foreland basin, Foreland basins, pp. 77–90, 1986.

D'Arcy, M., Whittaker, A. C., and Roda-Boluda, D. C.: Measuring alluvial fan sensitivity to past climate changes using a self-similarity

965   approach to grain-size fining, Death Valley, California, Sedimentology, 64, 388–424, 2017.
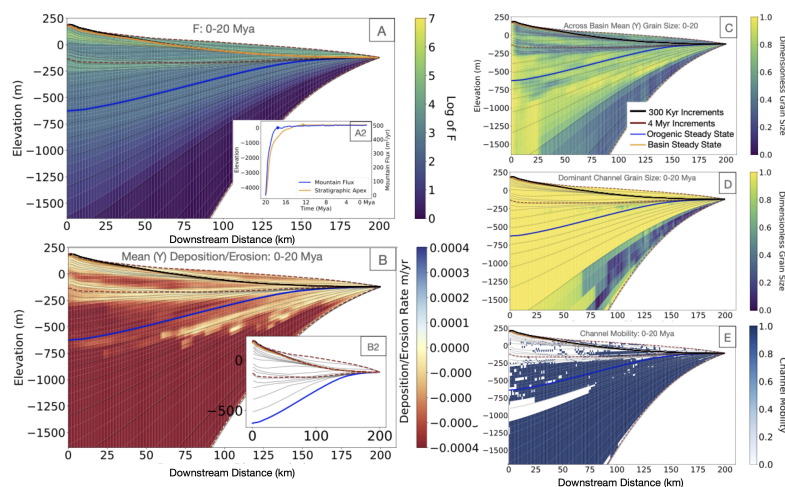
Figure A5. Basin evolution of F (A), deposition and erosion (B), mean grain size (C), dominant channel grain size (D), and channel mobility (E) is shown under a set-up with a higher β (through orogen precipitation) and a lower K (allowing for more rapid evolution to steady-state (where there are less local minima) and due to the higher imposed mean precipitation) than that in the main text. Shown in B2, after the basin reaches a constant and max. fan apex height (orange line in panel A2), there is a multi-million year period with little to no deposition. This appears as a strong black line as stratigraphic packages overlap as an unconformity. Eventually, the profile begins infilling again in the outer reaches of the basin. The simulation ran for 20Myrs (1000yr time step), with a K=2e-5, G=1, 50 km orogen, 200 km basin (1000 m cell length), Uplift of 0.01 myr^-1, elastic thickness of 20e3, asthenosphere density of 3200, lithosphere density of 2800, basin precipitation of 1, and an orogen precipitation of 20 producing a $\beta > \alpha$. After a log of F greater than 2, the basin is already in a high state of bypass where local minima no longer tend to dominate the basin based on figure 16. This is a theoretical example of an ancient basin that has long been at steady-state with an upstream (catchment) dominance in discharge to contrast with the foreland basin evolution shown in the main text.

Davy, P. and Lague, D.: Fluvial erosion/transport equation of landscape evolution models revisited, Journal of Geophysical Research: Earth Surface, 114, https://doi.org/https://doi.org/10.1029/2008JF001146, 2009.

DeCelles, P. G. and Giles, K. A.: Foreland basin systems, Basin research, 8, 105–123, 1996.

Dingle, E. H., Sinclair, H. D., Attal, M., Milodowski, D. T., and Singh, V.: <Subsidence control on river morphology and grain size in the
970   Ganga Plain.pdf>, https://doi.org/10.2475/08.2016.03, 2016.

Drew, F.: Alluvial and lacustrine deposits and glacial records of the Upper-Indus Basin, Quarterly Journal of the Geological Society, 29, 441–471, 1873.

Duller, R. A., Whittaker, A. C., Fedele, J. J., Whitchurch, A. L., Springett, J., Smithells, R., Fordyce, S., and Allen, P. A.: From grain size to tectonics, 115, https://doi.org/10.1029/2009jf001495, 2010.

975 Earle, S.: Physical geology, BCcampus, 2015.

Edmonds, D. A., Martin, H. K., Valenza, J. M., Henson, R., Weissmann, G. S., Miltenberger, K., Mans, W., Moore, J. R., Slingerland, R. L., Gibling, M. R., et al.: Rivers in reverse: Upstream-migrating dechannelization and flooding cause avulsions on fluvial fans, Geology, 50, 37–41, 2022.

Farrell, K. M.: Geomorphology, facies architecture, and high-resolution, non-marine sequence stratigraphy in avulsion deposits, Cumberland
980   Marshes, Saskatchewan, Sedimentary Geology, 139, 93–150, 2001.

Fedele, J. J. and Paola, C.: Similarity solutions for fluvial sediment fining by selective deposition, 112, https://doi.org/10.1029/2005jf000409,
2007.

Flemings, P. B. and Jordan, T. E.: A synthetic stratigraphic model of foreland basin development, Journal of Geophysical Research: Solid
Earth, 94, 3851–3866, 1989.

985   Grasso, D. N.: Hydrology of modern and late Holocene lakes, Death Valley, California, vol. 95, US Department of the Interior, US Geological
Survey, 1996.

Guerit, L., Yuan, X.-P., Carretier, S., Bonnet, S., Rohais, S., Braun, J., and Rouby, D.: Fluvial landscape evolution controlled by the sediment
deposition coefficient: Estimation from experimental and natural landscapes, Geology, 47, 853–856, 2019.

Hajek, E. A. and Straub, K. M.: Autogenic sedimentation in clastic stratigraphy. Annual Review of Earth and Planetary Sciences, 45, 681-
990   709., https://doi.org/10.1146/annurev-earth-, 2017.

Hammond, W. C., Blewitt, G., Li, Z., Plag, H.-P., and Kreemer, C.: Contemporary uplift of the Sierra Nevada, western United States, from
GPS and InSAR measurements, Geology, 40, 667–670, 2012.

Harries, R. M., Kirstein, L. A., Whittaker, A. C., Attal, M., and Main, I.: Impact of recycling and lateral sediment input on grain size fining
trends—Implications for reconstructing tectonic and climate forcings in ancient sedimentary systems., Basin Research, 31, 866–891, 2019.

995 Henderson, F.: Open Channel Flow, MacMillan, New York, iSBN 9780023535109, 1966.

Hill, J., Wood, R., Curtis, A., and Tetzlaff, D. M.: Preservation of forcing signals in shallow water carbonate sediments, Sedimentary Geology,
275, 79–92, 2012.

Hooke: Steady-state relationships on arid-region alluvial fans in closed basins., American Journal of Sciences, 266, 609–629, 1968.

Jablonski, B. V. and Dalrymple, R. W.: Recognition of strong seasonality and climatic cyclicity in an ancient, fluvially dominated, tidally
1000   influenced point bar: Middle McMurray Formation, Lower Steepbank River, north-eastern Alberta, Canada, Sedimentology, 63, 552–585,
2016.

Johnson, M. F. and Dalrymple, R. W.: Alluvial terracing in a falling-stage braidplain: the lower Cretaceous Cadomin Formation, west-central
Alberta, Canada, Journal of Sedimentary Research, 89, 701–727, 2019.

Koohzare, A., Vaníček, P., and Santos, M.: Pattern of recent vertical crustal movements in Canada, Journal of Geodynamics, 45, 133–145,
1005   2008.

Lai, J. and Huppert, K.: Asymmetric glaciation, divide migration, and postglacial fluvial response times in the Qilian Shan, Geology, 51,
860–864, 2023.

Leckie, D. A. and Cheel, R.: Sedimentology and depositional history of Lower Cretaceous coarse-grained elastics, southwest Alberta and
southeast British Columbia, Bulletin of Canadian Petroleum Geology, 45, 1–24, 1997.

1010 Leckie, D. A. and Nadon, G. C.: Evolution of Fluvial Landscapes in the Western Canada Foreland Basin: Late Jurassic to the Modern, Natural
Resources Canada, Geological Survey of Canada, 1997.

Leckie, D. A. and Smith, D. G.: Regional setting, evolution, and depositional cycles of the Western Canada Foreland Basin: Chapter 1, 1992.

Leeder, M. R., Harris, T., and Kirkby, M. J.: Sediment supply and climate change: implications for basin stratigraphy, Basin research, 10,
7–18, 1998.

1015   Leonard, J. S. and Whipple, K. X.: Influence of spatial rainfall gradients on river longitudinal profiles and the topographic expression of spatially and temporally variable climates in mountain landscapes, Journal of Geophysical Research: Earth Surface, 126, e2021JF006 183, 2021.

Lindsay, J. B.: Efficient hybrid breaching-filling sink removal methods for flow path enforcement in digital elevation models, Hydrological Processes, 30, 846–857, 2016.

1020   Ludvigson, G., Joeckel, R., Murphy, L., Stockli, D., González, L., Suarez, C., Kirkland, J., and Al-Suwaidi, A.: The emerging terrestrial record of Aptian-Albian global change, Cretaceous research, 56, 1–24, 2015.

Mackey, S. D. and Bridge, J. S.: Three-dimensional model of alluvial stratigraphy; theory and applications, Journal of Sedimentary Research, 65, 7–31, 1995.

McLean, J.: The Cadomin Formation: stratigraphy, sedimentology, and tectonic implications, Bulletin of Canadian Petroleum Geology, 25,
1025   792–827, 1977.

Mossop, G. and Shetsen, I., c.: Geological atlas of the Western Canada sedimentary basin, Canadian Society of Petroleum Geologists and Alberta Research Council, https://ags.aer.ca/reports/atlas-western-canada-sedimentary-basin, 1994.

Nicholas, A. P. and Quine, T. A.: Modeling alluvial landform change in the absence of external environmental forcing, Geology, 35, 527–530, 2007.

1030   Norton, I.: Two-stage formation of Death Valley, Geosphere, 7, 171–182, 2011.

Paola, C. and Voller, V. R.: A generalized Exner equation for sediment mass balance, Journal of Geophysical Research: Earth Surface, 110, n/a–n/a, https://doi.org/10.1029/2004jf000274, 2005.

Paola, C., Heller, P. L., and Angevine, C. L.: The large-scale dynamics of grain-size variation in alluvial basins, 1: Theory, Basin research, 4, 73–90, 1992.

1035   Parker, G., Paola, C., Whipple, K. X., Mohrig, D., Toro-Escobar, C. M., Halverson, M., and Skoglund, T. W.: Alluvial fans formed by channelized fluvial and sheet flow. II: Application, Journal of Hydraulic Engineering, 124, 996–1004, 1998.

Poulton, T., Tittemore, J., and Dolby, G.: Jurassic strata of northwestern (and west-central) Alberta and northeastern British Columbia, Bulletin of Canadian Petroleum Geology, 38, 159–175, 1990.

Price: Simulations of Alluvial Fan Deposition by a Random Walk Model, Water Resources Research, 16, 1974.

1040   Quick, L., Creed, M. J., Sinclair, H. D., Attal, M., Borthwick, A. G., and Sinha, R.: Hyperconcentrated floods cause extreme gravel transport through the sandy rivers of the Gangetic Plains, Communications Earth & Environment, 4, 297, 2023.

Rice, S. P.: The nature and controls on downstream fining within sedimentary links. Journal of Sedimentary Research, 69(1), 32-39., 1999.

Romans, B. W., Castelltort, S., Covault, J. A., Fildani, A., and Walsh, J. P.: Environmental signal propagation in sedimentary systems across timescales, Earth-Science Reviews, 153, 7–29, https://doi.org/10.1016/j.earscirev.2015.07.012, 2016.

1045   Scheingross, J. S., Limaye, A. B., McCoy, S. W., and Whittaker, A. C.: The shaping of erosional landscapes by internal dynamics, Nature Reviews Earth and Environment, 1, 661–676, https://doi.org/10.1038/s43017-020-0096-0, 2020.

Simpson, G. and Castelltort, S.: Coupled model of surface water flow, sediment transport and morphological evolution, Computers & Geosciences, 32, 1600–1614, 2006.

Skelly, R. L., Bristow, C. S., and Ethridge, F. G.: Architecture of channel-belt deposits in an aggrading shallow sandbed braided river: the
1050   lower Niobrara River, northeast Nebraska, Sedimentary Geology, 158, 249–270, 2003.

Smith, D. and Leckie, D.: The Paleogeographic Evolution of the Western Canada Foreland Basin, Bulletin of Canadian Petroleum Geology, 38, 181–181, 1990.

Sømme, T. O., Helland-Hansen, W., Martinsen, O. J., and Thurmond, J. B.: Relationships between morphological and sedimentological parameters in source-to-sink systems: a basis for predicting semi-quantitative characteristics in subsurface systems, Basin Research, 21, 361–387, https://doi.org/10.1111/j.1365-2117.2009.00397.x, 2009.

Stouthamer, E. and Berendsen, H. J.: Avulsion: the relative roles of autogenic and allogenic processes, Sedimentary Geology, 198, 309–325, 2007.

Straub, K. M. and Esposito, C. R.: Influence of water and sediment supply on the stratigraphic record of alluvial fans and deltas: Process controls on stratigraphic completeness, Journal of Geophysical Research: Earth Surface, 118, 625–637, 2013.

Tofelde, S., Bernhardt, A., Guerit, L., and Romans, B. W.: Times associated with source-to-sink propagation of environmental signals during landscape transience, Frontiers in Earth Science, 9, 628 315, 2021.

Turcotte, D. L. and Schubert, G.: Geodynamics, Cambridge university press, 2002.

Veldkamp, A., Baartman, J. E. M., Coulthard, T. J., Maddy, D., Schoorl, J. M., Storms, J. E. A., Temme, A. J. A. M., van Balen, R., van De Wiel, M. J., van Gorp, W., Viveen, W., Westaway, R., and Whittaker, A. C.: Two decades of numerical modelling to understand long term fluvial archives: Advances and future perspectives, Quaternary Science Reviews, 166, 177–187, https://doi.org/10.1016/j.quascirev.2016.10.002, 2017.

Walk, J., Stauch, G., Bartz, M., Brückner, H., and Lehmkuhl, F.: Geomorphology of the coastal alluvial fan complex Guanillos, northern Chile, Journal of Maps, 15, 436–447, 2019.

Walk, J., Stauch, G., Reyers, M., Vásquez, P., Sepulveda, F. A., Bartz, M., Hoffmeister, D., Brueckner, H., and Lehmkuhl, F.: Gradients in climate, geology, and topography affecting coastal alluvial fan morphodynamics in hyperarid regions–The Atacama perspective, Global and Planetary Change, 185, 102 994, 2020.

Walsh, E., Caracciolo, L., Ravidà, D., Burrough, S., and Thomas, D.: Holocene fluvial depositional regimes of the Huab River, Skeleton Coast, Namibia, Earth Surface Processes and Landforms, 47, 1820–1844, 2022.

Whipple, K. X. and Tucker, G. E.: Implications of sediment-flux-dependent river incision models for landscape evolution, Journal of Geophysical Research: Solid Earth, 107, ETG–3, 2002.

White, J. M. and Leckie, D. A.: Palynological age constraints on the Cadomin and Dalhousie formations in SW Alberta, Bulletin of Canadian Petroleum Geology, 47, 199–222, 1999.

Whittaker, A. C., Duller, R. A., Springett, J., Smithells, R. A., Whitchurch, A. L., and Allen, P. A.: Decoding downstream trends in stratigraphic grain size as a function of tectonic subsidence and sediment supply, Geological Society of America Bulletin, 123, 1363–1382, https://doi.org/10.1130/b30351.1, 2011.

Yuan, X. P., Braun, J., Guerit, L., Rouby, D., and Cordonnier, G.: A New Efficient Method to Solve the Stream Power Law Model Taking Into Account Sediment Deposition, Journal of Geophysical Research: Earth Surface, 124, 1346–1365, https://doi.org/10.1029/2018jf004867, 2019.